

Dissipative Tunneling Rates through the Incorporation of First-Principles Electronic Friction in Instanton Rate Theory II: Benchmarks and Applications

Y. Litman,^{1, a)} E. S. Pócs,¹ C. L. Box,² R. Martinazzo,³ R. J. Maurer,² and M. Rossi^{1, b)}

¹⁾MPI for the Structure and Dynamics of Matter, Luruper Chaussee 149, 22761 Hamburg, Germany

²⁾Department of Chemistry, University of Warwick, Coventry CV4 7AL, United Kingdom

³⁾Department of Chemistry, Università degli Studi di Milano, Via Golgi 19, 20133 Milano, Italy

(Dated: 11 March 2022)

In part I, we presented the ring-polymer instanton with explicit friction (RPI-EF) method and showed how it can be connected to the *ab initio* electronic friction formalism. This framework allows the calculation of tunneling reaction rates that incorporate the quantum nature of the nuclei and certain types of non-adiabatic effects (NAEs) present in metals. In this second part, we analyze the performance of RPI-EF on model potentials and apply it to realistic systems. For a 1D double-well model, we benchmark the method against numerically exact results obtained from multi-layer multi-configuration time-dependent Hartree calculations. We demonstrate that RPI-EF is accurate for medium and high friction strengths and less accurate for extremely low friction values. We also show quantitatively how the inclusion of NAEs lowers the cross-over temperature into the deep tunneling regime, reduces the tunneling rates, and in certain regimes, steers the quantum dynamics by modifying the tunneling pathways. As a showcase of the efficiency of this method, we present a study of hydrogen and deuterium hopping between neighboring interstitial sites in selected bulk metals. The results show that multidimensional vibrational coupling and nuclear quantum effects have a larger impact than NAEs on the tunneling rates of diffusion in metals. Together with part I, these results advance the calculations of dissipative tunneling rates from first principles.

I. INTRODUCTION

The transport kinetics of small molecules and atoms in metals play an important role in technological applications in several areas, like fuel cells, batteries, and nuclear reactors, among others^{1–4}. In particular, accurate measurements of hydrogen diffusion are still experimentally challenging since diffusion coefficients are very sensitive to the microstructure of the material and the composition of the alloy^{5–7}. As a consequence, reported values of diffusion constants by different groups can be scattered over a few orders of magnitude.

First-principles calculations have the potential to provide an increased understanding of the transport dynamics of light particles in well-defined structures throughout a wide range of thermodynamic conditions (e.g., temperature and pressure), which can complement experiments and guide further developments. Most of the atomistic calculations performed to study nuclear dynamical processes rely on Newtonian dynamics on the ground-state adiabatic potential energy surface (PES), as given by the Born-Oppenheimer approximation (BOA). However, the coupling of the nuclear movement with electrons in the metal can easily induce electronic excitations, which represent a breakdown of the BOA and give rise to non-adiabatic effects (NAEs)^{8,9}. Furthermore, light particles such as hydrogen and deuterium can exhibit strong nuclear quantum effects (NQE), which can either increase or decrease its mobility through metals^{10,11}. As a consequence, an under-

standing of the interplay of NQEs and NAEs in the transport process of light atoms in realistic systems remains elusive.

Several exact methods to simulate non-adiabatic quantum dynamics have been developed in the last decades^{12–14}. However, due to the unfavorable scaling of these theoretical approaches with the number of degrees of freedom, efficient but accurate methods are required to capture NQEs and NAEs in high-dimensional systems or to be used with costly *ab initio* potentials. In part I of this paper, we presented the ring-polymer instanton with explicit friction (RPI-EF) theory for the calculation of dissipative thermal tunneling rates, which has the potential to fulfill these requirements. Briefly, RPI-EF allows an easy and efficient incorporation of the electronic friction formalism, originally proposed by Hellsing and Persson¹⁵ and Head-Gordon and Tully¹⁶, into the semi-classical ring-polymer instanton (RPI) rate theory¹⁷.

In this article, we show the merits and limitations of RPI-EF. We benchmark the accuracy of RPI-EF rate predictions by comparing them with numerically exact theories in model potentials. Subsequently, we examine the interplay of the reaction barrier height and friction strengths on the tunneling rate in 1D and 2D model potentials connected to a bath. Finally, the new approach is applied to hydrogen and deuterium hopping reactions in bulk transition metals, focusing on Pd, by employing Kohn-Sham density functional theory. These calculations allow a quantitative analysis of the impact of different effects on the rate constants, such as the dimensionality of the system, NQEs, and NAEs.

Part II of this paper is structured as follows: In Section II the methods employed to obtain the tunneling rates are briefly summarized and the simulation details for each one are specified. In Section III, the model potentials and the systems

^{a)}Electronic mail: yairlitman@gmail.com

^{b)}Electronic mail: mariana.rossi@mpsdl.mpg.de

treated from first-principles are described. Results of numerical simulations on low-dimensional models for position-independent and position-dependent friction tensors are discussed in Section IV A and IV B, respectively. Finally, the first-principles results for the hydrogen and deuterium hopping in metals are discussed in Section V. Section VI concludes by summarizing the main results and giving an outlook to future directions.

II. RATE CALCULATION METHODS

A. Ring-polymer instanton (with explicit friction) calculations

The RPI rate theory^{18,19} is a semi-classical method that allows the calculation of tunneling rates. RPI theory can be interpreted as the extension of Eyring transition state theory (TST)²⁰ into the deep tunneling regime, since the rates are evaluated utilizing only a limited amount (often a single) special configuration, circumventing the necessity of real-time sampling. While in TST this special configuration is the first-order saddle-point connecting reactants and products on the potential energy surface (PES), in RPI rate theory the special configurations are found at the first-order saddle-points of the extended space of the ring polymer (RP) potential. These trajectories in imaginary time are known as instanton trajectories. The RPI rate expression is analogous to the one proposed by TST and reads,

$$k_{\text{inst}}(\beta) \propto e^{-U_P^{\text{sys}}(\bar{q})/\hbar}, \quad (1)$$

where

$$U_P^{\text{sys}}(\mathbf{q}) = \sum_{k=1}^P \sum_{i=1}^{3N} m_i \frac{\omega_P^2}{2} (q_i^{(k)} - q_i^{(k+1)})^2 + \sum_{k=1}^P V(q_1^{(k)}, \dots, q_{3N}^{(k)}) \quad (2)$$

is the RP potential. In the previous equation, $q_i^{(k)}$ is the position of the i -th degree of freedom of the k -th bead of the ring polymer, m_i is the mass of the i -th degree of freedom, N is the number of atoms, P is the number of beads (replicas), \mathbf{q} is an abbreviated notation to represent all the degrees of freedom, \bar{q} denotes the instanton geometry, and $\omega_P = (\beta_P \hbar)^{-1}$ with $\beta_P = \frac{1}{k_B P T}$.

In part I, we showed how RPI rate theory can be extended to compute tunneling rates for systems connected to a harmonic bath which simulates a dissipative environment. Irrespective of the dissipative mechanism, and assuming that the environment degrees of freedom adjust adiabatically to the system position, one can fully characterize the system-environment coupling by a position (\mathbf{q}) and frequency (λ) dependent friction tensor, $\tilde{\eta}(\mathbf{q}, \lambda)$. Moreover, when the frequency and position dependence are decoupled, we proved that the RP potential

that enters Eq. 1 is renormalized, adopting the form

$$U_P^{\text{MF}} = U_P^{\text{sys}} + \sum_{l=-P/2+1}^{P/2} \sum_{i=1}^{3N} \frac{\omega_l}{2} \left[\sum_{k=1}^P C_{lk} \left(\int_{\mathbf{q}^{\text{ref}}}^{\mathbf{q}^{(k)}} \tilde{\eta}(\mathbf{q}', \omega_k)^{1/2} \cdot d\mathbf{q}' \right) \right]^2, \quad (3)$$

where $\omega_l = 2\omega_P \sin(|l|\pi/P)$ are the free RP normal mode frequencies and C is the transformation matrix between the RP normal modes and Cartesian coordinates. In the limiting case of a position-independent friction, the previous expression can be simplified to

$$U_P^{\text{MF}} = U_P^{\text{sys}} + \sum_{l=-P/2+1}^{P/2} \sum_{i=1}^{3N} \frac{\tilde{\eta}(\omega_l) \omega_l}{2} (Q_i^{(l)})^2, \quad (4)$$

where $Q^{(l)}$ represent the free RP normal mode coordinates.

The RPI calculations were performed using the i-PI²¹ code. The forces and energies required by the algorithm were passed to i-PI from an external code through an interface based on internet sockets. The RPI-EF calculations required an extension of the i-PI communication protocol. We added to the existing communication of the energy, forces, and stresses from external codes to i-PI, the possibility to pass additional information as JSON-formatted strings. In this way, it is possible to communicate any type of data and, more importantly, when the data is numeric, it becomes available to be used by any implemented algorithm within i-PI. This enables the use of quantities beyond energies and forces, that change along the simulation, within different types of dynamics.

The FHI-aims code²² and an in-house python code were used in connection to i-PI for the DFT and model calculations, respectively. Transition-state geometries were obtained either by the string method²³ combined with the climbing image technique²⁴ or using a minimum-mode-following algorithm²⁵, as implemented in i-PI. The RPI calculations were initialized after finding the transition state, by stretching the transition-state geometry along the mode with imaginary frequency using a number of replicas between 10 and 16. Optimizations were started at a temperature of 10 K below the corresponding cross-over temperature, T_c° . After converging the instanton pathway for the first calculation, successive steps of temperature decrease and RP interpolation to increase the number of beads were performed until the target temperature was reached. If required, further calculations with more beads were performed to guarantee that, in all cases and for all temperatures, the final rates were converged within a 10% error^{26,27}. See more details in section I of the Supplemental Information (SI).

B. Multi-configuration time-dependent Hartree Calculations

Numerically exact results for selected models in this paper were obtained with the multi-layer variant^{28–30} of the multi-configuration time-dependent Hartree method^{31–33} (ML-MCTDH), as implemented in the Heidelberg package³⁴.

MCTDH is a variational method that relies on optimal, time-dependent basis functions to alleviate the exponential scaling problem of standard methods based on direct expansions on time-independent basis. In the MCTDH *ansatz* the wave function $|\Psi(t)\rangle$ is expanded on orthogonal configurations $|\Phi_J(t)\rangle$, which in turn are products of ‘single particle’ functions (SPFs),

$$|\Psi(t)\rangle = \sum_J A_J(t) |\Phi_J(t)\rangle = \sum_J A_J(t) \prod_k |\phi_{j_k}^{(k)}(t)\rangle, \quad (5)$$

and both the expansion coefficients (A_J) and the SPFs ($|\phi_{j_k}(t)\rangle$) are variationally optimized. Here, $J = (j_1, \dots, j_k, \dots, j_F)$ is a multi-index, the index $k = 1, 2, \dots, F$ runs over the single-particles, and $j_k = 1, \dots, n_k$ labels the SPFs used for the k^{th} mode. Conventional MCTDH uses single-particles for each degree of freedom or small groups thereof, and represents their SPFs by a direct expansion on a grid/basis-set (the so-called primitive grid) designed for the single particle at hand. This limits its capability of handling large systems. In contrast, in ML-MCTDH the single particles are high-dimensional modes whose SPFs are described by further MCTDH expansions employing lower dimensional SPFs. The procedure can be indefinitely iterated till reasonably small single-particles are defined that can be described on primitive grids. This recipe, similarly to tensor networks and matrix-product states³⁵, endows the wave function with a hierarchical, flexible structure that allows the treatment of considerably larger systems. In particular, ML-MCTDH has been successfully applied to the calculation of thermal rate constants in condensed-phase problems^{36,37} in the framework of the reactive flux-side approach, where $k(T)$ is given by the long-time limit of the equilibrium flux-side time-correlation function^{38,39}.

In this work, we followed closely the original work by Wang and Thoss^{40,41}, who introduced an importance sampling technique to recast the trace expression of the flux-side correlation function as an accessible ensemble-average over time-evolving wavepackets. In a nutshell, the evaluation of the rate constant is reduced to: i) a preparation step where the wavepackets are initialized by combining (system) Boltzmannized flux eigenvectors with bath states drawn from the canonical ensemble of the uncoupled bath, ii) an equilibration step where imaginary-time dynamics introduces the correlations present in the coupled system, and iii) a propagation step where the real-time dynamics is followed up to the onset of the kinetic regime (the long-time limit alluded to above). Details about the calculations, including an overview of the flux-side approach, the Monte Carlo sampling, the tree structure of the ML-MCTDH wavefunction, the number of SPFs and the primitive grids used, are provided in section II of SI. Converged calculations were obtained with 50 bath modes and using 128-256 realizations for each value of T and coupling strength.

III. SIMULATION DETAILS AND PARAMETERS

A. 1D and 2D double well models

We analyze the performance of RPI-EF on a double-well model similar to the ones usually employed to study quantum dynamics in system-bath models^{42,43}. The potential energy surface of the system is given by

$$V_{\text{DW}}(q) = -\frac{1}{2}m\omega^{\ddagger 2}(q - q_0)^2 + \frac{m^2\omega^{\ddagger 4}}{16V_0}q^4, \quad (6)$$

where, unless otherwise specified, we set m as the mass of atomic hydrogen and $\omega^{\ddagger} = 500 \text{ cm}^{-1}$. The coupling between the system and the bath can be made position-dependent according to⁴⁴

$$f(q) = q[1 + \varepsilon_1 \exp(-\Delta q^2/2) + \varepsilon_2 \tanh(\Delta q)], \quad (7)$$

where $\Delta q = (q - q^{\ddagger})/\delta$, δ determines the length-scale of the nonlinear couplings, and ε_1 and ε_2 the magnitude of its symmetric and anti-symmetric components, respectively. The calculations with position-independent friction were obtained by setting $\varepsilon_1 = \varepsilon_2 = 0$. Naturally, the position-dependent couplings of real systems do not generally adopt such simple forms. However, as it will be shown in Sec. IV B, this simplified form will prove sufficient to expose the importance of including this position-dependence in the tunneling rates.

We consider an Ohmic (linear) spectral density multiplied by an exponential cutoff, leading to

$$\tilde{\eta}_{ii}(\mathbf{q}, \lambda) = \frac{2}{\pi} \int_0^{+\infty} d\omega \tilde{\eta}_0 \left(\frac{\partial f(\mathbf{q})_i}{\partial q_i} \right)^2 \frac{\lambda}{\omega^2 + \lambda^2} e^{-\omega/\omega_c} \quad (8)$$

where $\tilde{\eta}_0$ is the static friction coefficient and, unless otherwise specified, we set $\omega_c = 500 \text{ cm}^{-1}$.

To illustrate the tensorial nature of the friction we also considered a two-dimensional double double-well (DDW) potential given by

$$V_{\text{DDW}}(q_1, q_2) = V_{\text{DW}}(q_1) + V_{\text{DW}}(q_2) + Cq_1q_2, \quad (9)$$

where C is a constant to be specified. Additionally, for the sake of simplicity we considered that the bath couples to each degree of freedom independently, and the coupling function is given by

$$f(q_1, q_2) = (f(q_1), f(q_2)) \quad (10)$$

where $f(q_i)$ is given by Eq. 7.

B. Fcc metals

We also perform first-principles atomistic simulations to showcase the methodology developed in this paper. More specifically, we focus on hydrogen and deuterium hopping reactions within interstitial sites in different bulk fcc metals: Pd,

Pt, Cu, and Ag. The bulk systems were modelled by $2 \times 2 \times 2$ cubic supercells containing one hydrogen or deuterium atom and 32 metal atoms. Energies and forces were computed employing density-functional theory (DFT) using the FHI-aims²² code and the Perdew, Burke, and Ernzerhof (PBE) exchange-correlation functional⁴⁵. Geometries were relaxed using the standard *light* settings (in the case of Pd, increasing the radial multiplier to 2) from FHI-aims until all forces were below 10^{-3} eV/Å. Minimum-energy pathways (MEP) were obtained with the string method²³ combined with the climbing image technique²⁴ as implemented in the aimsChain package provided with the FHI-aims code. The BFGS algorithm was used as the optimization procedure and the residual forces converged below 10^{-3} eV/Å. Unless specified otherwise, a $6 \times 6 \times 6$ k-point sampling was used. This setup ensures that errors in relative energies are below 1 meV/atom. We obtained lattice constants of 3.95 Å, 3.97 Å, 3.63 Å, and 4.16 Å, for Pd, Pt, Cu and Ag, respectively, in good agreement with Ref.⁴⁶. See section III A of the SI for more details regarding convergence tests.

As explained in part I of this paper, the electronic friction tensor was computed as

$$\tilde{\eta}_{ij}(\mathbf{q}, \lambda) = \hbar \sum_{\nu, \nu'} \langle \psi_{\nu} | \partial_i \psi_{\nu'} \rangle \langle \psi_{\nu'} | \partial_j \psi_{\nu} \rangle (f(\epsilon_{\nu}) - f(\epsilon_{\nu'})) \times \frac{\lambda \Omega_{\nu\nu'}}{\lambda^2 + \Omega_{\nu\nu'}^2}, \quad (11)$$

where $f(\epsilon)$ is the state occupation given by the Fermi-Dirac distribution, ψ_{ν} and ϵ_{ν} are the KS electronic orbitals and orbital energies of the ν -th level, i and j label the nuclear degrees of freedom, $\partial_i = \partial/\partial q_i$, and $\Omega_{\nu\nu'} = (\epsilon_{\nu} - \epsilon_{\nu'})/\hbar$. The calculation of the non-adiabatic coupling elements was obtained through a finite-difference approach, as currently implemented in the FHI-aims code⁴⁷. We stress that Eq. 11 is different from the expression commonly used in the literature^{16,47–50}. We used a step length of 0.001 Å for the finite-difference evaluation, and a $16 \times 16 \times 16$ k-point sampling for the friction tensor. We only calculated the tensor components related to the hydrogen or deuterium atoms. More details regarding convergence tests can be found in section III. B of the SI.

IV. NUMERICAL RESULTS ON MODEL POTENTIALS

A. Position-independent friction

We start by analyzing the linear coupling case and benchmarking the RPI-EF results against the ML-MCTDH results. In Fig. 1 the rate constants calculated for the DW potential (Eq. 6) at different temperatures and friction values are shown. The RPI-EF results are in good agreement with the exact calculations for $\tilde{\eta}_0/m\omega^{\ddagger} > 0.1$ at all the temperatures considered. We note that the lowest temperature, 50 K, represents less than half of the cross-over temperature evaluated

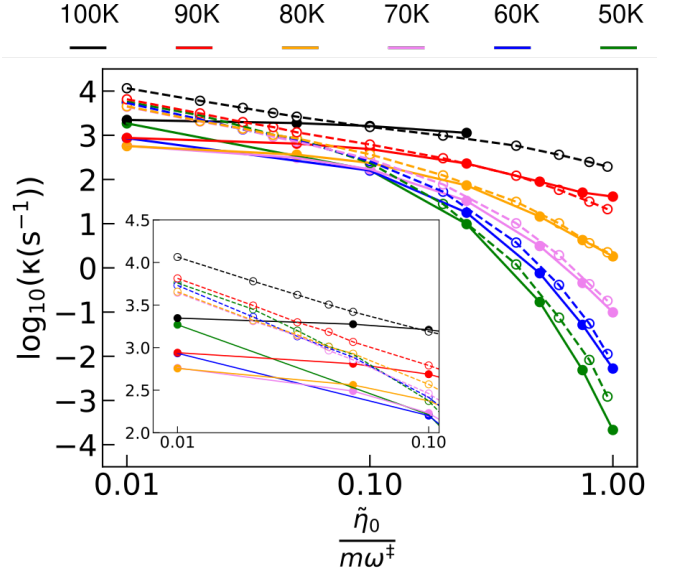


FIG. 1. Reaction rate constants for the DW potential ($V_0 = 258$ meV, $\omega_c = 500$ cm⁻¹ and $q_0 = 0$) for temperatures between 50 K and 100 K for different friction values computed with RPI-EF (solid lines with filled circles) and ML-MCTDH (dashed lines with empty circles).

without friction. Even at considerably higher friction values, where the RPI approach has been predicted to be inadequate⁵¹, the agreement is quite remarkable, showing that real-time dynamical effects, such as recrossing, play a minor role in these cases. At lower friction values, specially below $\tilde{\eta}_0/m\omega^{\ddagger} = 0.05$, the agreement deteriorates. The poor performance of the RPI-EF method in the weak coupling regime is not surprising since RPI predicts a finite value for the rate even at $\tilde{\eta}_0 = 0$, where the dynamics in such a 1D model would be described by a Rabi oscillation and, strictly speaking, a rate process cannot be defined. Indeed, RPI-EF reaches a plateau at $\tilde{\eta}_0/m\omega^{\ddagger} \approx 0.05$ which might be interpreted as “an intrinsic” dissipation inherent to that theory, as a consequence of considering trajectories that bounce only once in the evaluation of the imaginary time kernel¹⁷. When η goes to zero, the exact results approach the limit of coherent tunneling dynamics, yielding ML-MCTDH rates that are larger than the ones calculated with RPI. In passing, we note that both methods present a minimum of the rate at around 70 K in the weak-friction regime (see inset in Fig. 1), which differs from the low-temperature power law observed in metastable systems^{52,53}. A deeper study of this subtle but interesting quantum effect is beyond the scope of the current work and will be the subject of future research.

One way to evaluate the relative importance of tunneling to the total rate is to analyze the tunneling enhancement factor, κ^{tun} , defined as

$$\kappa^{\text{tun}}(\beta, \tilde{\eta}) = \frac{k_{\text{inst}}(\beta, \tilde{\eta})}{k_{\text{TST}}(\beta, \tilde{\eta})} \quad (12)$$

with $k_{\text{TST}}(\beta, \eta)$ being the TST rate²⁶. Figs. 2 and 3 show the calculated tunneling enhancement factors for different barrier

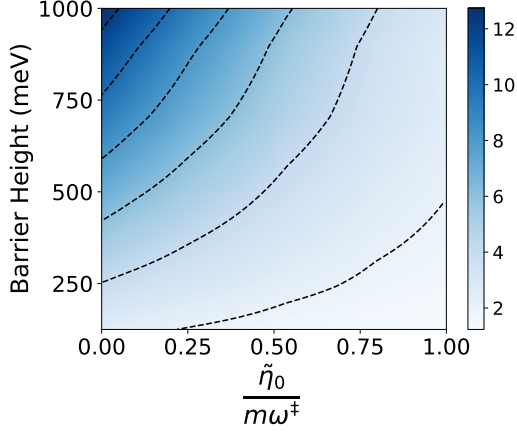


FIG. 2. Tunneling enhancement factors $\log_{10}[\kappa(\beta, \tilde{\eta}_0)]$ as a function of energy barrier height and friction strength, on the DW potential with $q_0 = 0.0 \text{ \AA}$ (symmetric reaction profile) at $T = 0.7T_c^\circ = 80 \text{ K}$. The colour-scale is logarithmic and contour lines are drawn for isosurfaces spaced by 2 logarithmic units.

heights and friction values for symmetric and asymmetric reactions, respectively. For the range of parameters considered here, it can be observed that the tunneling enhancement factor calculated with and without friction can differ up to almost ten orders of magnitude, that it increases with the increase of the barrier height, and that it decreases with increasing friction strength. For barriers larger than 500 meV, the isosurfaces are approximately straight lines with slope one, meaning that barrier heights and friction strengths have a comparable but opposite effect on tunneling.

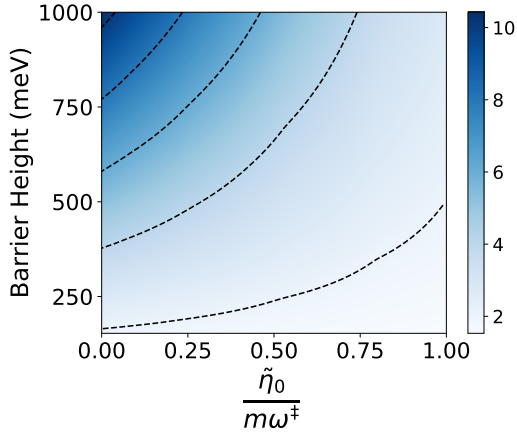


FIG. 3. Same as Fig. 2 with $q_0 = 0.08 \text{ \AA}$ (asymmetric reaction profile). The exoergic reaction is considered.

We now proceed to discuss why the friction strength and the barrier height impact the tunneling contribution to the rate. The friction value determines the system-bath coupling strength. As evidenced by $\kappa^{\text{tun}} \sim 1$ at higher friction values, the stronger the coupling, the more classical the system behaves. However, the reason why the impact of the friction becomes more relevant at higher barrier heights is less straight-

forward to understand and requires the analysis of the instanton pathways. In Fig. 4, we show the decomposition of the instanton geometry into the free RP normal mode basis. We first consider the case without coupling to the bath. For symmetric barriers, Fig. 4a, the instanton pathway expands only along the odd RP normal modes due to the symmetry of the underlying potential, and the first two degenerate RP normal modes ($l = \pm 1$) contribute with more than 99% to the path. For asymmetric barriers, Fig. 4c, even though all normal modes are in principle allowed by symmetry, the first two degenerate RP normal modes exhibit the highest contribution, with the centroid mode ($l = 0$) presenting a non-negligible contribution as well. For both barrier shapes, the population of the $l = \pm 1$ modes increases with the barrier height, simply because the pathway from reactants to product becomes longer. The same trends are observed for calculations with intermediate system-bath coupling, Fig. 4c and 4d, where the only difference is an overall smaller population of the RP normal modes due to the shorter instanton pathway. Thus, higher barriers correlate with a relatively larger impact of the friction on the rate. This is due to an increase in the RP normal mode population, which leads to an increase of the last term in Eq. 4.

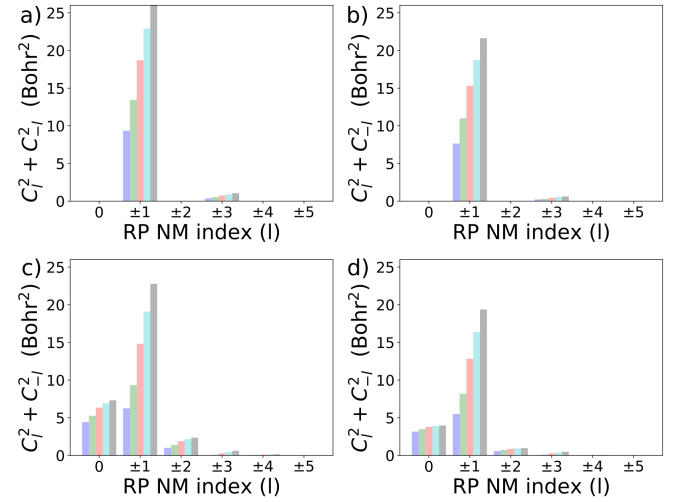


FIG. 4. Decomposition of instanton geometry into the free RP normal mode basis at a representative temperature of $T = 0.70T_c^\circ = 80 \text{ K}$ for (a) symmetric DW with $\tilde{\eta}_0/m\omega^\ddagger = 0.00$, (b) symmetric DW with $\tilde{\eta}_0/m\omega^\ddagger = 0.50$, (c) asymmetric DW ($q_0 = 0.08 \text{ \AA}$) with $\tilde{\eta}_0/m\omega^\ddagger = 0.00$, and (d) asymmetric DW ($q_0 = 0.08 \text{ \AA}$) with $\tilde{\eta}_0/m\omega^\ddagger = 0.50$. Five different barrier heights were considered: 125 meV (purple), 258 meV (green), 500 meV (red), 750 meV (light blue), and 1000 meV (gray). Coefficients are ordered and grouped by their corresponding RP normal mode (NM) index (l).

Grote-Hynes (GH) theory^{54–56} defines a relationship between reaction rates obtained with a finite friction strength and those obtained with vanishing friction strength in the classical limit. In part I of this article, we showed an extension of GH theory to the deep tunneling regime for the case of position-independent friction. Briefly, we proposed that tunneling rates with finite friction strength – RPI-EF rates – at a given temperature, can be related to tunneling rates without friction –

RPI rates – performed at a scaled temperature. The scaling relation for the temperatures is given by

$$T_b/T_c^\circ = \sqrt{\left(\frac{\tilde{\eta}(\omega_l^b)}{2m\omega^\ddagger}\right)^2 \frac{1}{l^2} + \left(\frac{T_a}{T_c^\circ}\right)^2} - \frac{\tilde{\eta}(\omega_l^b)}{2m\omega^\ddagger} \frac{1}{l} \quad (13)$$

where T_c° is the cross-over temperature without friction, T_b the target temperature at which the RPI-EF result is desired, T_a the temperature at which the RPI calculation must be performed, and ω_l^b the l free RP normal mode frequency at T_b . Since ω_l^b depends on T_b , this equation has to be solved self-consistently. Even though Eq. 13 must be fulfilled for all l , from Fig. 4 one can expect that considering only $\omega_{l=\pm 1}$ should be a good assumption.

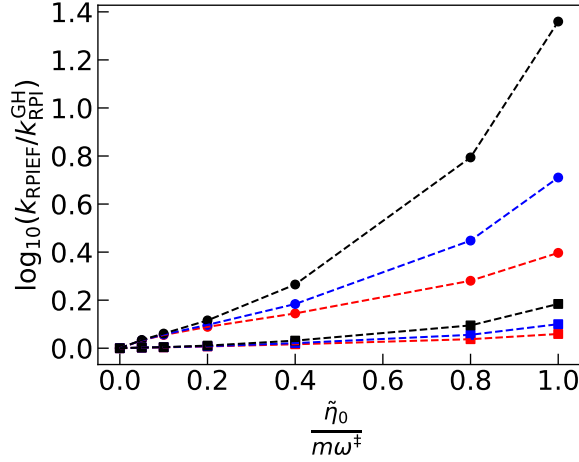


FIG. 5. Error on the RPI rate values obtained by the scaling relation shown in Eq. 13 ($k_{\text{RPI}}^{\text{GH}}$), compared to RPI-EF rates (k_{RPIEF}). The error is reported as the logarithm of the ratio between these rates in the symmetric DW model. Temperatures of $0.70T_c^\circ$ (squares) and $0.557T_c^\circ$ (circles), and reaction barriers of 258 meV (red), 500 meV (blue), and 1000 meV (black) are shown. An analogous plot for an asymmetric barrier is presented in the SI.

In Fig. 5, the error obtained by computing the rate, using only $\omega_{l=\pm 1}$ in Eq. 13, for different temperatures and coupling strengths in the symmetric DW potential is presented. The estimated RPI rates at the scaled temperatures are within one order of magnitude from the full RPI-EF rates for all friction strengths, but they are in better agreement for $\tilde{\eta}_0/m\omega^\ddagger < 0.5$. Similar accuracy is observed for an asymmetric DW model with this approximation, even though the $l = 0$ mode is appreciably activated (see section IV in the SI).

B. Position-Dependent Friction

We now consider the case where the coupling between the system and the bath depends on the position of the system coordinate, i.e. a position-dependent friction. Fig. 6 shows instanton pathways obtained for different system-bath coupling strengths on a DDW potential, as described by Eq. 9, at a temperature considerably lower than T_c° in this model.

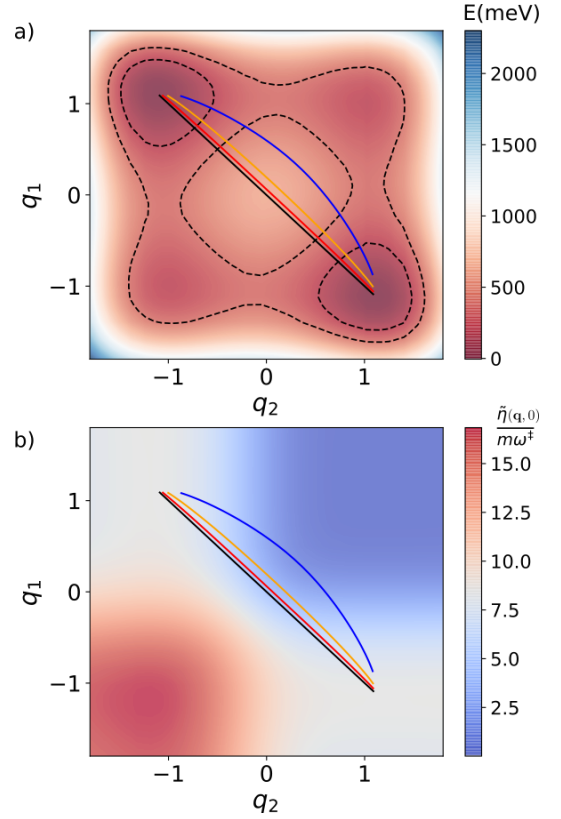


FIG. 6. Instanton pathways obtained at 40 K using the DDW model with $V_0 = 258$ meV, $q_0 = 0$ Å, $C = 97.1$ meV/Å² (0.001 a.u.), $\epsilon_1 = 0$, $\epsilon_2 = -0.8$, and $\Delta = 1.0$ for $\tilde{\eta}_0/m\omega^\ddagger = 0, 0.10, 0.25$, and 0.50 represented by full black, red, orange, and blue lines, respectively. The pathways are shown on top of a) a heat map representing the underlying potential energy surface b) a heat map that helps visualize the position-dependence of the friction tensor. The map is computed as the sum of the diagonal elements of $\tilde{\eta}$ for $\tilde{\eta}_0/m\omega^\ddagger = 0.50$ (see Eq. 8 and 10 in the main text).

The parameters of the model were chosen such that the PES presents two global minima, two local minima, four first order saddle points that connect each global minimum with the closest local minimum, and one second order saddle point at $(q_1, q_2) = (0, 0)$, as shown in Fig. 6a. The optimal tunneling pathway in the absence of dissipation is represented by the black curve in Fig. 6 and it is a linear trajectory that connects the two global minima by crossing the second order saddle point. For $\tilde{\eta} > 0$, the anisotropy of the friction (see Fig. 6b) results in a modification of the instanton pathway, which bends towards regions of lower friction values. The magnitude of the bending of this path increases as the strength of the friction becomes larger. This shows that the optimal dissipative tunneling pathway is a compromise between the path with the shortest length, the path with the lowest potential energy, and the path with lowest friction. Indeed, for $\tilde{\eta}_0/m\omega^\ddagger > 0.5$, the dissipation is so strong close to the second-order saddle point that no instanton pathway that connects directly the two global minima can be found.

V. HOPPING OF HYDROGEN AND DEUTERIUM IN BULK METALS

A. Minimum energy paths, barrier heights and friction strengths

Having characterized the performance of RPI-EF in model potentials, we now address the interplay of NAEs and NQEs on the hopping reaction of H within bulk metals, which we calculate from first-principles electronic-structure simulations.

We first analyze the MEP of the reactions in Pd, Pt, Cu, Ag and Al. We note that we focus on the hopping reaction between neighboring octahedral→tetrahedral interstitial sites. Even though in perfect solids these reactions determine the diffusion rate, in real materials other mechanisms might become the rate determining step of the diffusion process^{57,58}. In Table I, we report the reaction energy, reaction barrier, and electronic-friction values along the MEP for the reactions considered in this work. As shown in column 3, the energy barriers are in the 100-300 meV range, in accordance with previous studies⁵⁹.

System	E_{T-O} (meV)	E_{TS-O} (meV)	$\tilde{\eta}$ (ps ⁻¹)	T_c° (K)	ω^\ddagger (cm ⁻¹)
H@Pd	43	148	0.7 - 2.7	115	501
H@Pt	-35	44	0.8 - 2.8	96	420
H@Cu	188	300	0.7 - 1.1	140	612
H@Ag	52	160	0.7 - 1.0	116	504
H@Al	-71	88	1.8 - 3.1	84	365

TABLE I. Reaction energy, $E_{T-O} = E_T - E_O$, and energy barrier heights, $E_{TS-O} = E_{TS} - E_O$, for the different fcc metals considered in this work. E_T , E_O , and E_{TS} refer to the potential energy corresponding to structures where the H atom is located at the tetrahedral (T), octahedral (O) and transition state (TS) sites, respectively. Values are reported without ZPE corrections. Minimum and maximum values adopted by the electronic friction, $\tilde{\eta}$, along the MEP are presented in column four. Values are evaluated at 54 meV (which corresponds to the first non-zero ring-polymer normal mode frequency at 100 K) and considering a projection of $\tilde{\eta}$ on the reaction coordinate. Columns 5 and 6 show the crossover temperature, T_c° , and imaginary frequency at the TS, ω^\ddagger , respectively.

We continue by analyzing the electronic friction tensor $\tilde{\eta}_{il}(q, \lambda)$ on the hydrogen atom along the MEPs. In Fig. 7a, we present the electronic friction values evaluated at the first non-zero ring-polymer normal mode frequency at 100 K, projected onto the direction parallel to the reaction coordinate for the case of Pd. The friction values vary up to almost an order of magnitude, indicating the necessity of having a rate theory that takes into account such position dependence. The electronic friction along the MEP for the other metals shows a strong position dependence as well (see section III B of the SI). As shown in column 4 of Table I, the values vary from 0.7 ps⁻¹ to 3.1 ps⁻¹. The magnitude of the friction coefficients is large enough to impact vibrational lifetimes⁴⁷, adsorption mechanisms⁶⁰, and scattering experiments^{60,61}. However, the dimensionless coefficient $\tilde{\eta}/m\omega^\ddagger$ yields at most a value of 0.05 (for Al), which, given the relatively low barrier heights, would result in a reduction

of the tunneling rates by less than a factor of 5, according to our study on model potentials presented in the previous sections (see Figs. 2 and 3).

A closer look at the expression used to compute the electronic friction tensor, Eq. 11, allows us to rationalize the reasons behind such small coefficients⁶². Large friction values will arise in the case of a high DOS close to the Fermi level and due to the presence of hydrogen states close to the Fermi level. The former contributes to Eq. 11 via the Fermi-Dirac factors, the latter contributes via the strength of the nonadiabatic coupling. While the former depends mainly on the metal at hand, the latter is affected by both the impurity and the metal⁶³. We analyzed the atomic projected DOS (see section III C in the SI) and confirmed that Pd and Pt are, at the same time, the systems that present the largest electronic friction values and the highest DOS at the Fermi level among the transition metals. Surprisingly, Al presents slightly larger friction values, without a high DOS at the Fermi energy. This might suggest that the nonadiabatic couplings are comparatively large in this case. However, in all cases, the hydrogen atom neither creates new states nor affects the DOS appreciably in the vicinity of the Fermi level, which ultimately leads to rather small friction coefficients along the MEP for these systems.

Up to this point, we have considered values of the friction tensor at a single frequency. However, the calculation of the tunneling rates require the evaluation of the friction tensor at all the RP normal modes frequencies (Eq. 3), and more importantly in the derivation of RPI-EF with a position-dependent friction tensor, we have assumed that a separable coupling *ansatz* is valid. This *ansatz* is equivalent to assuming that the frequency dependence of the friction tensor remains the same at all (relevant) positions. As an illustrative example, we present in Fig. 7b the frequency dependence of the friction tensor at the stationary points of the MEP (reactant, transition and product state) for the hydrogen hopping reaction in Pd. The frequency dependence shows a non-monotonic profile with a maximum around 0.6 eV and remains fairly similar along the MEP suggesting that the non-adiabatic couplings in bulk metals are, to a great extent, well described by a “separable coupling”. This observation is equally valid for the other metals (see SI section III B). A different type of coupling might be observed in scattering reactions, where atoms or molecules transition from vacuum to electron-rich environments^{60,64}. As discussed in section IV A, only the first few ring-polymer normal modes are appreciably activated. For this reason, only a relatively small fraction of spectral density contributes to the rates (see Fig. 7b).

B. Tunneling rates: The case of Pd

We performed full-dimensional instanton calculations on Pd in order to gauge the predictive power of our studies on low-dimensional models and static estimators presented in the previous sections. We selected Pd because it presents high values of friction along the MEP and the diffusion of H in Pd has been well studied theoretically and experimentally before. In

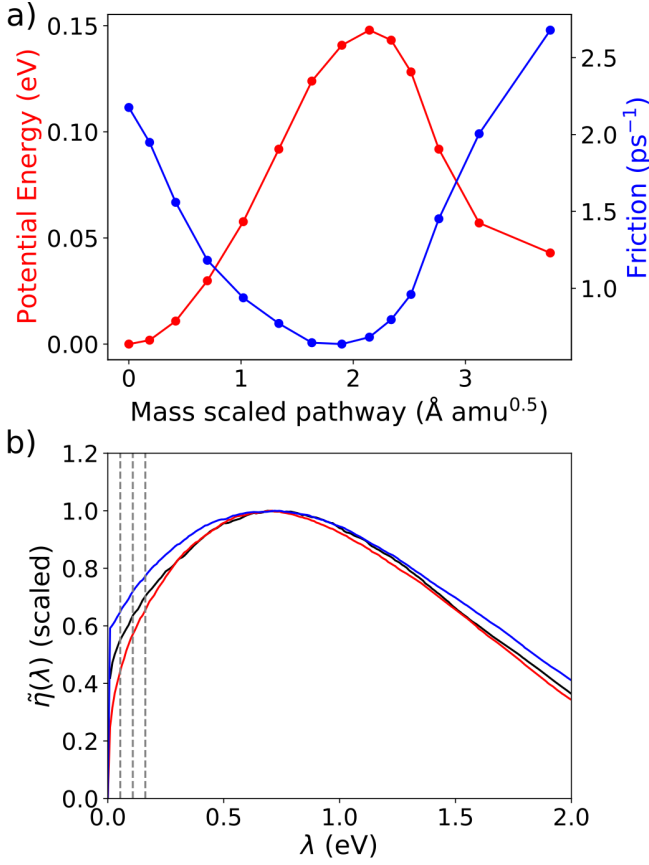


FIG. 7. a) Minimum energy pathway (MEP) and friction along the reaction coordinate for the H hopping reaction in Pd. The energy is set to zero at the reactant geometry. b) Frequency dependence of the friction tensor projected on the reaction coordinate at the reactant (black), transition state (red), and product (blue) states. To ease visual comparison, all curves in panel b have been scaled to adopt the value of 1 at the highest friction value. The first three non-zero ring-polymer normal modes frequencies at 100K are depicted as vertical dashed gray lines.

order to reduce the computational cost, we performed instanton calculations on a fcc cubic cell containing 4 Pd atoms and 1 H or D atom. These calculations were performed using a $12 \times 12 \times 12$ k-point sampling. The relatively small size of the unit cell induces an effective increase of the barrier when compared to larger unit cells and the new T_c° increases to 136 K (see section I in the SI). Since larger barriers magnify the effect of the friction on the rates, these calculations can be considered an upper-limit estimation of the impact of the friction on these rates.

In Fig. 8, the reaction rates for the hopping reaction of H and D in Pd from the octahedral to the tetrahedral site using TST, RPI theory and RPI-EF theory are presented. At temperatures below T_c° , the tunneling effects, evidenced by the difference between the RPI and TST rates, become increasingly important, enhancing the rate by several orders of magnitude. The comparison of the TST predictions for H and D indicates an inverse kinetic isotope effect (KIE). The inverse KIE can be

traced back to the softening of the normal modes orthogonal to the reaction pathway at the transition-state geometry⁶⁵. Since this effect is mainly due to ZPE, it is also present at temperatures above T_c and has been reported experimentally⁵. Below T_c , the emergence of tunneling creates a competition between ZPE and tunneling effects as already reported by Shiga *et al.*⁶⁶. Moreover, the similarity of the reaction rates for both isotopologues around 80 K is in agreement with the results of Ref.⁶⁶ and with experiments. However, the absolute values reported here are considerably smaller as a consequence of the rather small unit-cell employed in the calculations.

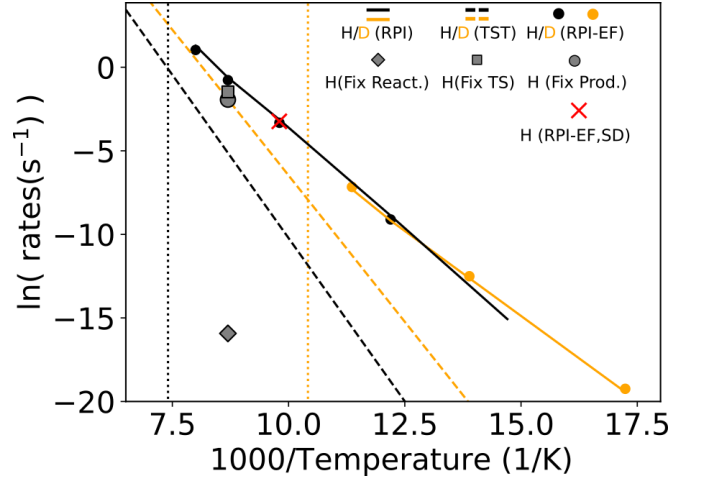


FIG. 8. Reaction rates for octahedral→tetrahedral-site hopping reaction of H (black) and D (orange) in Pd, calculated by TST (dashed lines), and RPI rate theory (solid lines). RPI-EF rates with position-independent friction, fixed at a value of 4 ps^{-1} , are shown by black and orange circles for H and D, respectively, while the RPI-EF rates with position-dependent friction is depicted as a red cross. RPI rate calculations with the Pd atoms fixed at their reactant, transition and product states are presented by diamond, square and circle gray symbols, respectively. T_c° for H and D are marked by vertical black and orange dotted lines, respectively.

We now inspect the impact of the lattice on the reaction rates. For this purpose, we performed RPI calculations where the Pd atoms were fixed at the reactant, product and transition state positions at 115 K. The rate obtained when the Pd atoms are fixed at their reactant positions is 7 and 4 orders of magnitude slower than the RPI and TST estimates, respectively. This confirms the significant contribution of the lattice fluctuations to the reactive process¹⁰ and highlights the multidimensional nature of the reaction. In contrast, the rate estimates obtained from the calculations with the Pd atoms fixed at their transition-state or product positions are within an order of magnitude of the RPI estimates. The former result is expected since we are analyzing the rates at only 20 K below T_c° , such that the instanton pathway lies very close to the TS geometry. The latter result, instead, shows that the lattice relaxation between the transition state and the product is of comparatively lower relevance.

Finally, we consider the effect of the electronic friction on the rate. At 100 K, we performed a calculation with on-the-fly estimations of the friction tensor along the instanton path-

way (also included in the instanton optimization). In order to gauge the importance of the spatial dependence of the friction, we also performed, at the same temperature, an instanton calculation using a constant value of 4 ps^{-1} for the friction (slightly higher than the maximum value reported in Table I). The results were numerically indistinguishable within the accuracy of our calculations, which may seem an unexpected result, at first. We proceeded to perform calculations with a constant and spatially-independent friction value (which is less computationally demanding) at several other temperatures. In Figure 8, we show these results and, as predicted by our earlier assessment, the friction coefficients are not large enough to produce a significant effect on the rates. This explains why the spatial dependence also does not appreciably change the rate constants.

VI. CONCLUSIONS

We have benchmarked the RPI-EF method and showed its performance in model potentials and first-principles calculations. By performing numerically exact simulations in 1D model systems including a spatially-independent friction, we showed that RPI-EF yields accurate rates for all but very small friction coefficients at a much reduced computational cost. A systematic analysis of 1D and 2D double-well potentials allowed us to determine the magnitude of the decrease of the tunneling rates caused by friction, as a function of the coupling strength and barrier height. We found that the suppression of tunneling is promoted by high coupling strengths and high energy barriers. We were also able to demonstrate that for a spatially-dependent friction tensor, the instanton pathway can be considerably deformed towards low-friction regions, when compared to the “non-dissipative” path (without friction). In comparison to previous similar approaches^{67,68}, the RPI-EF method is advantageous because it is highly-efficient, more intuitive and mathematically simpler.

In the context of reactions involving atoms and molecules in metallic environments, RPI-EF allows the inclusion of NQEs and NAEs as described by an effective electronic friction. While here we used an electronic friction formulation that disregards electronic correlation^{16,47,48}, the RPI-EF approach is rather general and can be combined with other flavours of electronic friction that go beyond the independent quasiparticle picture. As a consequence of the relatively low computational cost of both RPI and the employed *ab initio* electronic friction formalism, RPI-EF allows the study of high-dimensional systems with on-the-fly *ab initio* evaluation of the forces and the electronic friction tensor.

In this work, we presented calculations of hydrogen and deuterium hopping between nearest interstitial sites of selected fcc metals, employing density-functional theory calculations. By evaluating the impact that different factors have on the reactions rates of this reaction in bulk Pd, we established that nuclear tunneling and lattice relaxation play a larger role in determining the magnitude of the rate than electronic friction. The latter turned out to have a negligible impact on the reaction rates of these systems. This negative result, how-

ever, answers an important theoretical question regarding the interplay between NAEs (modeled by electronic friction) and NQEs⁶⁹, and also validates the rate constants currently used in this context for multiscale modeling⁷⁰. Nonetheless, we anticipate that for impurities or adsorbates that present electronic levels in the vicinity of the Fermi energy of the metal, NAEs might play a more prominent role in connection with tunneling. We also expect to observe a larger effect for lighter particles such as Muons⁷¹, or for surface reactions with higher energy barriers⁷².

ACKNOWLEDGMENTS

Y.L., E.S.P. and M.R. acknowledge financing from the Max Planck Society and computer time from the Max Planck Computing and Data Facility (MPCDF). Y.L. and M.R. thank Jeremy Richardson, Aaron Kelly, and Stuart Althorpe for a critical reading of the manuscript. C.L.B. acknowledges financial support through an EPSRC-funded PhD studentship. R.M. acknowledges Unimi for granting computer time at the CINECA HPC center. R.J.M. acknowledges financial support through a Leverhulme Trust Research Project Grant (RPG-2019-078) and the UKRI Future Leaders Fellowship programme (MR/S016023/1).

¹R. Mohtadi and S.-i. Orimo, Nat. Rev. Mater. **2**, 16091 (2016).

²I. M. Robertson, P. Sofronis, A. Nagao, M. L. Martin, S. Wang, D. W. Gross, and K. E. Nygren, Metall. Mater. Trans. B **46**, 1085 (2015).

³A. Traidia, E. Chatzidouros, and M. Jouiad, Corros. Rev. **36**, 323 (2018).

⁴L. Schlappach and A. Züttel, Nature **414**, 353 (2001).

⁵J. Völkl and G. Alefeld, “Diffusion of hydrogen in metals,” in *Hydrogen in Metals I: Basic Properties*, edited by G. Alefeld and J. Völkl (Springer Berlin Heidelberg, Berlin, Heidelberg, 1978) pp. 321–348.

⁶S. Jothi, T. Croft, and S. Brown, Int. J. Hydrog. Energy **40**, 2882 (2015).

⁷“Diffusion,” in *The Metal-Hydrogen System: Basic Bulk Properties* (Springer Berlin Heidelberg, Berlin, Heidelberg, 2005) pp. 303–400.

⁸H. Nienhaus, Surf. Sci. Rep. **45**, 1 (2002).

⁹A. M. Wodtke, Chem. Soc. Rev. **45**, 3641 (2016).

¹⁰H. Kimizuka, S. Ogata, and M. Shiga, Phys. Rev. B **97**, 014102 (2018).

¹¹H. Kimizuka and M. Shiga, Phys. Rev. Mater. **5**, 065406 (2021).

¹²M. Beck, A. Jäckle, G. Worth, and H.-D. Meyer, Phys. Rep. **324**, 1 (2000).

¹³Y. Tanimura and R. Kubo, J. Phys. Soc. Japan **58**, 101 (1989).

¹⁴G. Ilk and N. Makri, J. Chem. Phys. **101**, 6708 (1994).

¹⁵B. Hellsing and M. Persson, Phys. Scr. **29**, 360 (1984).

¹⁶M. Head-Gordon and J. C. Tully, J. Chem. Phys. **103**, 10137 (1995).

¹⁷J. O. Richardson, Int. Rev. Phys. Chem. **37**, 171 (2018).

¹⁸J. O. Richardson and S. C. Althorpe, J. Chem. Phys. **131**, 214106 (2009).

¹⁹A. Arnaldsson, *Calculation of quantum mechanical rate constants directly from ab initio atomic forces*, Ph.D. thesis, University of Washington (2007).

²⁰H. Eyring, J. Chem. Phys. **3**, 107 (1935).

²¹V. Kapil, M. Rossi, O. Marsalek, R. Petraglia, Y. Litman, T. Spura, B. Cheng, A. Cuzzocrea, R. H. Meißner, D. M. Wilkins, B. A. Helfrecht, P. Juda, S. P. Bienvenue, W. Fang, J. Kessler, I. Poltavsky, S. Vandenbrande, J. Wieme, C. Corminboeuf, T. D. Kühne, D. E. Manolopoulos, T. E. Markland, J. O. Richardson, A. Tkatchenko, G. A. Tribello, V. V. Speybroeck, and M. Ceriotti, Comp. Phys. Comm. **236**, 214 (2019).

²²V. Blum, R. Gehrke, F. Hanke, P. Havu, V. Havu, X. Ren, K. Reuter, and M. Scheffler, Comp. Phys. Comm. **180**, 2175 (2009).

²³W. E. W. Ren, and E. Vanden-Eijnden, J. Chem. Phys. **126**, 164103 (2007).

²⁴G. Henkelman, B. P. Uberuaga, and H. Jónsson, J. Chem. Phys. **113**, 9901 (2000).

²⁵J. Nichols, H. Taylor, P. Schmidt, and J. Simons, J. Chem. Phys. **92**, 340 (1990).

- ²⁶A. N. Beyer, J. O. Richardson, P. J. Knowles, J. Rommel, and S. C. Althorpe, *J. Phys. Chem. Lett.* **7**, 4374 (2016).
- ²⁷Y. Litman, *Tunneling and Zero-Point Energy Effects in Multidimensional Hydrogen Transfer Reactions: From Gas Phase to Adsorption on Metal Surfaces*, Ph.D. thesis, Freie Universität Berlin (2020).
- ²⁸H. Wang and M. Thoss, *J. Chem. Phys.* **119**, 1289 (2003).
- ²⁹U. Manthe, *J. Chem. Phys.* **130**, 054109 (2009).
- ³⁰O. Vendrell and H.-D. Meyer, *J. Chem. Phys.* **134**, 044135 (2011).
- ³¹H.-D. Meyer, U. Manthe, and L. S. Cederbaum, *Chem. Phys. Lett.* **165**, 73 (1990).
- ³²M. H. Beck, A. Jäckle, G. A. Worth, and H.-D. Meyer, *Phys. Rep.* **324**, 1 (2000).
- ³³H.-D. Meyer, F. Gatti, and G. A. Worth, eds., *Multidimensional Quantum Dynamics: MCTDH Theory and Applications* (Wiley-VCH, Weinheim, 2009).
- ³⁴G. A. Worth, M. H. Beck, A. Jäckle, O. Vendrell, and H.-D. Meyer, The MCTDH Package, Version 8.5 (2013), <http://mctdh.uni-hd.de/>.
- ³⁵J. I. Cirac, D. Pérez-García, N. Schuch, and F. Verstraete, *Rev. Mod. Phys.* **93**, 045003 (2021).
- ³⁶H. Wang, D. E. Skinner, and M. Thoss, *J. Chem. Phys.* **125**, 174502 (2006).
- ³⁷I. R. Craig, M. Thoss, and H. Wang, *J. Chem. Phys.* **127**, 144503 (2007).
- ³⁸W. H. Miller, S. D. Schwartz, and J. W. Tromp, *The Journal of Chemical Physics* **79**, 4889 (1983).
- ³⁹W. H. Miller, *Journal of Physical Chemistry A* **102**, 793 (1998).
- ⁴⁰H. Wang, D. E. Skinner, and M. Thoss, *The Journal of Chemical Physics* **125**, 174502 (2006).
- ⁴¹I. R. Craig, M. Thoss, and H. Wang, *Journal of Chemical Physics* **127** (2007), 10.1063/1.2772265.
- ⁴²M. Topaler and N. Makri, *J. Chem. Phys.* **101**, 7500 (1994).
- ⁴³I. R. Craig and D. E. Manolopoulos, *J. Chem. Phys.* **122**, 0 (2005).
- ⁴⁴J. B. Straus, J. M. Gomez Llorente, and G. A. Voth, *J. Chem. Phys.* **98**, 4082 (1993).
- ⁴⁵J. P. Perdew, K. Burke, and M. Ernzerhof, *Phys. Rev. Lett.* **77**, 3865 (1996).
- ⁴⁶P. Haas, F. Tran, and P. Blaha, *Phys. Rev. B* **79**, 085104 (2009).
- ⁴⁷R. J. Maurer, M. Askerka, V. S. Batista, and J. C. Tully, *Phys. Rev. B* **94**, 115432 (2016).
- ⁴⁸W. Dou, G. Miao, and J. E. Subotnik, *Phys. Rev. Lett.* **119**, 046001 (2017).
- ⁴⁹A. C. Luntz and M. Persson, *J. Chem. Phys.* **123**, 074704 (2005).
- ⁵⁰S. Monturet and P. Saalfrank, *Phys. Rev. B* **82**, 075404 (2010).
- ⁵¹J. O. Richardson and S. C. Althorpe, *J. Chem. Phys.* **131**, 214106 (2009).
- ⁵²H. Grabert, U. Weiss, and P. Hanggi, *Phys. Rev. Lett.* **52**, 2193 (1984).
- ⁵³H. Grabert, P. Olschowski, and U. Weiss, *Phys. Rev. B* **36**, 1931 (1987).
- ⁵⁴R. F. Grote and J. T. Hynes, *J. Chem. Phys.* **73**, 2715 (1980).
- ⁵⁵R. F. Grote and J. T. Hynes, *J. Chem. Phys.* **74**, 4465 (1981).
- ⁵⁶E. Pollak, *J. Chem. Phys.* **85**, 865 (1986).
- ⁵⁷D. Di Stefano, M. Mrovec, and C. Elsässer, *Acta Mater.* **98**, 306 (2015).
- ⁵⁸A. Pedersen and H. Jónsson, *Acta Mater.* **57**, 4036 (2009).
- ⁵⁹P. Ferrin, S. Kandoi, A. U. Nilekar, and M. Mavrikakis, *Surf. Sci.* **606**, 679 (2012).
- ⁶⁰O. Bünermann, H. Jiang, Y. Dorenkamp, A. Kandratsenka, S. M. Janke, D. J. Auerbach, and A. M. Wodtke, *Science* **350**, 1346 (2015).
- ⁶¹A. Kandratsenka, H. Jiang, Y. Dorenkamp, S. M. Janke, M. Kammmer, A. M. Wodtke, and O. Bünermann, *Proc. Natl. Acad. Sci. USA* **115**, 680 (2018).
- ⁶²M. Forsblom and M. Persson, *J. Chem. Phys.* **127**, 154303 (2007).
- ⁶³L. Lecroart, N. Hertl, Y. Dorenkamp, H. Jiang, T. N. Kitsopoulos, A. Kandratsenka, O. Bünermann, and A. M. Wodtke, *J. Chem. Phys.* **155**, 034702 (2021).
- ⁶⁴R. J. Maurer, B. Jiang, H. Guo, and J. C. Tully, *Phys. Rev. Lett.* **118**, 256001 (2017).
- ⁶⁵J. Meisner and J. Kästner, *Angew. Chem. Int. Ed.* **55**, 5400 (2016).
- ⁶⁶H. Kimizuka, S. Ogata, and M. Shiga, *Phys. Rev. B* **100**, 024104 (2019).
- ⁶⁷A. Caldeira and A. Leggett, *Ann. Phys.* **149**, 374 (1983).
- ⁶⁸U. Weiss, *Quantum Dissipative Systems*, 3rd ed. (WORLD SCIENTIFIC, 2008).
- ⁶⁹W. Dou and J. E. Subotnik, *J. Chem. Phys.* **148**, 230901 (2018).
- ⁷⁰C. Hüter, P. Shanthraj, E. McEniry, R. Spatschek, T. Hickel, A. Tehranchi, X. Guo, and F. Roters, *Metals* **8** (2018).
- ⁷¹H. Teichler, *Phys. Lett. A* **64**, 78 (1977).
- ⁷²E. del V. Gómez, S. Amaya-Roncancio, L. B. Avalle, D. H. Linares, and M. C. Gimenez, *Appl. Surf. Sci.* **420**, 1 (2017).

SUPPORTING INFORMATION:**Dissipative Quantum Tunneling Rates through the Incorporation of First-Principles Electronic Friction in Instanton Rate Theory**

Y. Litman,^{1, a)} E. S. Pócs,¹ C. L. Box,² R. Martinazzo,³ R. J. Maurer,² and M. Rossi^{1, b)}

¹⁾*MPI for the Structure and Dynamics of Matter, Luruper Chaussee 149,
22761 Hamburg, Germany*

²⁾*Department of Chemistry, University of Warwick, Coventry CV4 7AL,
United Kingdom*

³⁾*Department of Chemistry, Università degli Studi di Milano, Via Golgi 19,
20133 Milano, Italy*

(Dated: 11 March 2022)

^{a)}Electronic mail: yairlitman@gmail.com

^{b)}Electronic mail: mariana.rossi@mpsd.mpg.de

I. CONVERGENCE OF INSTANTON CALCULATIONS

The convergence tests for the tunneling rates were performed using a 2x2x2 orthorhombic supercell containing four Pd atoms since it is expected to present similar convergence behavior as an 8x8x8 orthorhombic supercell containing 32 Pd atoms. In Table SI the tunneling rates with varying number of beads is presented. We analyze the PT/T_c ratio where P is the number of beads, T the temperature and T_c the cross-over temperature as suggested in Ref.¹. We also report the T_c for H and D in tables SII and SIII. It can be seen that for all the temperatures considered, PT/T_c ratios of 36 and 72 deliver converged rates within 10% and 2%, respectively.

$T(K)$	T/T_c	P	PT/T_c	$k_{\text{inst}} \text{ (s}^{-1}\text{)}$
125	0.92	32	29.4	3.17
125	0.92	96	88	3.66
115	0.85	32	27.2	6.44(-1)
115	0.85	64	54.4	5.50(-1)
115	0.85	96	82	5.38(-1)
115	0.85	128	108	5.34(-1)
115	0.85	256	216	5.39(-1)
102	0.75	48	36	4.74(-2)
102	0.75	96	72	4.39(-2)
102	0.75	128	96	4.33(-2)
82	0.60	64	38	1.55(-4)
82	0.60	128	76	1.41(-4)
82	0.60	160	96	1.40(-4)
68	0.50	72	36	3.04(-7)
68	0.50	144	72	2.87(-7)
68	0.50	192	96	2.85(-7)

TABLE SI: Tunneling Rates for Pd₀₄H.

System	T_c (K)	ω_{TS} (cm^{-1})
Pd_{04}H	136	594
Pd_{16}H	123	537
Pd_{32}H	114	502

TABLE SII: Cross-over temperature (T_c) and imaginary frequency at the transition state (ω_{TS}). Pd_{32}H , Pd_{16}H , and Pd_{04}H , were computed with a k-grid mesh of 6x6x6, 6x6x6, and 12x12x12, respectively.

System	T_c (K)	ω_{TS} (cm^{-1})
Pd_{04}D	96	422
Pd_{16}D	87	381
Pd_{32}D	82	356

TABLE SIII: Cross-over temperature (T_c) and imaginary frequency at the transition state (ω_{TS}). Pd_{32}D , Pd_{16}D and Pd_{04}D , were computed with a k-grid mesh of 6x6x6, 6x6x6, and 12x12x12, respectively.

II. MCTDH CALCULATIONS

A. Flux-side approach

The thermal rate constant k_β of the isomerization reaction $A \rightleftharpoons B$ is traditionally expressed as the long time limit of a time-dependent “rate constant” $k_\beta(t)$, $k_\beta = \lim_{t \rightarrow \infty} k_\beta(t)^{2-4}$. The latter involves the so-called flux-side correlation function $C_{\text{fs}}^\beta(t)$ and, in its refined (improved) form⁵, reads as

$$k_\beta(t) = \frac{1}{Z_A} \frac{C_{\text{fs}}^\beta(t)}{P_A(0) + [P_A(0) - 1] \chi_\beta - \left(\frac{1}{Z_A} + \frac{1}{Z_B} \right) \int_0^t C_{\text{fs}}^\beta(\tau) d\tau}. \quad (1)$$

Here, h is the projection operator that separates the configuration space of the products from that of the reagents, Z_A and Z_B are, respectively, the reagent and product partition functions,

$$Z_A = \text{Tr} (e^{-\beta H} (1 - h)) \quad Z_B = \text{Tr} (e^{-\beta H} h)$$

$\chi_\beta = Z_A/Z_B$ is the inverse equilibrium constant of the reaction, $P_A(0)$ is the initial population of the reactants’ well

$$P_A(0) = 1 - \frac{1}{Z_A} \text{Tr} (e^{-\beta H/2} (1 - h) e^{-\beta H/2} h)$$

and

$$C_{\text{fs}}^\beta(t) = \text{Tr} (F_\beta h(t)) \quad (2)$$

is the above mentioned flux-side correlation function in its most popular, symmetrized form³. The latter is the key quantity and requires, besides h above, the Boltzmannized flux operator

$$F_\beta = e^{-\beta H/2} F e^{-\beta H/2} \quad F = \frac{i}{\hbar} [H, h] \quad (3)$$

which is the Boltzmannized version of the Heisenberg time derivative of h (*i.e.*, the flux operator F). In Eq. 1 the long time limit is the true infinite time limit (*i.e.*, the notation $t \rightarrow \infty$ is exact, with no *caveats*), although in practice the appropriate t is a macroscopically small time beyond which $k_\beta(t)$ approaches a constant value. Since most often it holds

$$P_A(0) \approx 1 \text{ and } \int_0^{t_P} C_{\text{fs}}(\tau) d\tau \ll \frac{Z_A Z_B}{Z_A + Z_B},$$

the rate takes the form

$$k_\beta \approx \frac{1}{Z_A} \lim_{t \rightarrow \infty} C_{\text{fs}}(t) \quad (4)$$

where now the limit needs to be interpreted at the *plateau* time t_P where the correlation function attains a constant value. Eq. 4 represents the celebrated “flux-side” expression of the thermal rate constant. For a derivation of Eq. 1 appropriate to a condensed-phase environment see Ref. 6.

B. Boltzmann sampling

We focus here on practical issues that arise when numerically evaluating the trace expressions of Eq. 2 for a condensed-phase problem involving many degrees of freedom^{7,8}. In particular, we describe the importance sampling scheme introduced by the authors of Ref.s 7 and 8 to turn the problem into an efficient Monte Carlo sampling of the state space. We shall first describe such ‘Monte Carlo wavepacket strategy’ for computing average values of observables and, later, highlight the amendments needed to evaluate the correlation functions.

In the following we assume that H takes the form $H = H_S + H_{\text{int}} + H_B$ where H_S is the system Hamiltonian, H_B is a sum of independent oscillator Hamiltonians and H_{int} the interaction term between the system and the bath. Accordingly, for the state space we have $\mathcal{H} = \mathcal{H}_S \otimes \mathcal{H}_B$, and we make use of vectors of the form $|n, N\rangle \equiv |n\rangle |N\rangle$ where $|n\rangle$ is an arbitrary system state and $|N\rangle$ an eigenstate of the bath, i.e., for $N = \{n_1 n_2 \dots n_k \dots\}$,

$$H_B |N\rangle = E_N |N\rangle \quad \text{and} \quad E_N = \sum_k \hbar \omega_k \left(n_k + \frac{1}{2} \right).$$

1. Averages of observables

The equilibrium average value of an operator A takes the form

$$\langle A \rangle = \frac{1}{Z} \text{Tr}(e^{-\beta H} A) \equiv \frac{1}{Z} \text{Tr}(e^{-\frac{\beta}{2} H} A e^{-\frac{\beta}{2} H}) = \frac{1}{Z} \sum_{n, N} \langle \Psi_{n, N}^\beta | A | \Psi_{n, N}^\beta \rangle$$

where $|\Psi_{n, N}^\beta\rangle = e^{-\frac{\beta}{2} H} |n, N\rangle$. This equation is best re-written in terms of *normalized* vectors $|\Phi_{n, N}^\beta\rangle$, which are those directly available from the MCTDH package upon imaginary-time evolution. Clearly, for a solution of the Bloch equation

$$-\frac{\partial |\Psi_\beta\rangle}{\partial \beta} = H |\Psi\rangle \quad |\Psi_{\beta=0}\rangle = |\Psi_0\rangle$$

given its squared norm $p(\beta) = \langle \Psi_\beta | \Psi_\beta \rangle$ and the energy expectation $\epsilon(\beta) = \langle \Psi_\beta | H | \Psi_\beta \rangle / p(\beta)$, we have $\frac{\partial p}{\partial \beta}(\beta) = -2\epsilon(\beta)p(\beta)$, hence $p(\beta) = e^{-2 \int_0^\beta \epsilon(\tau) d\tau}$ and $|\Psi_\beta\rangle = e^{-\int_0^\beta \epsilon(\tau) d\tau} |\Phi_\beta\rangle$. Thus,

$$\begin{aligned} \langle A \rangle &= \frac{1}{Z} \sum_{n,N} p_{n,N} \left(\frac{\beta}{2} \right) \langle \Phi_{n,N}^\beta | A | \Phi_{n,N}^\beta \rangle \\ &= \frac{Z_0}{Z} \sum_N \frac{e^{-\beta E_N}}{Z_0} \sum_n W_{n,N}(\beta) \langle A \rangle_{n,N}^\beta \end{aligned}$$

where Z_0 is the partition function of the uncoupled bath, $\langle A \rangle_{n,N}^\beta = \langle \Phi_{n,N}^\beta | A | \Phi_{n,N}^\beta \rangle$ are expectation values and

$$W_{n,N}(\beta) = e^{+\beta E_N} e^{-2 \int_0^{\beta/2} \epsilon_{n,N}(\tau) d\tau} \quad (5)$$

are thermal factors determined by the average energy $\epsilon_{n,N}(\tau)$ of the state $|\Phi_{n,N}^\tau\rangle$ during the imaginary-time evolution. The ensemble-average takes thus the form of a Boltzmann-weighted sum of terms which can be efficiently evaluated *via* Monte Carlo sampling,

$$\langle A \rangle = \frac{Z_0}{Z} \sum_n \langle \langle W_{n,N}(\beta) \langle A \rangle_{n,N}^\beta \rangle \rangle \quad (6)$$

where the double bracket denotes the Boltzmann average (and N is the corresponding random variable). This expression can be further rewritten upon noticing that $Z = Z_0 \sum_n \langle \langle W_{n,N}(\beta) \rangle \rangle$ (as it follows from Eq. 6 upon setting $A = 1$), hence

$$\langle A \rangle = \frac{\sum_n \langle \langle W_{n,N}(\beta) \langle A \rangle_{n,N}^\beta \rangle \rangle}{\sum_n \langle \langle W_{n,N}(\beta) \rangle \rangle} \quad (7)$$

which requires just one sampling.

In practice, given a basis of \mathcal{H}_S a number of bath configurations $|N_i\rangle$ are generated from the Boltzmann distribution and the vectors $|n, N_i\rangle$ are propagated in imaginary-time to compute the expectation values and the thermal factors. Sampling can be performed independently for each bath oscillator, using the known cumulative distributions $P_\nu = \sum_{k=0}^\nu \rho_k$ (where ρ_k are the Boltzmann probabilities) of a harmonic oscillator with frequency ω ,

$$P_\nu = 1 - e^{-\beta \hbar \omega (\nu+1)}.$$

That is, $\nu_i = \text{int}(-\ln(\xi_i/\beta \hbar \omega))$, for ξ_i random in $[0, 1]$, gives a set of quantum numbers ν_i Boltzmann distributed. Thus, besides bookkeeping issues, the procedure is entirely straightforward and generates vectors $|N_I\rangle \equiv |n_{i_1}\rangle |n_{i_2}\rangle \dots |n_{i_k}\rangle \dots |n_{i_F}\rangle$ where $I = (i_1 i_2 \dots i_k \dots i_F)$ and F

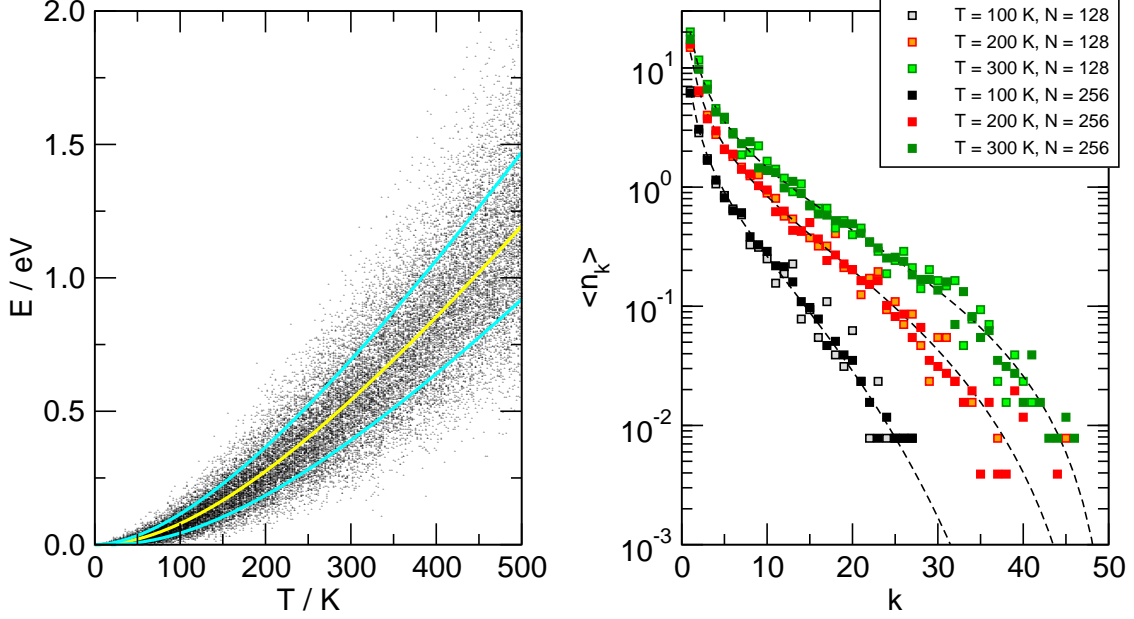


FIG. S1: Sampling of the bath (results for a typical bath containing $F = 50$ oscillators).

Left: individual energy of the bath states $|N_I\rangle$ sampled at different temperatures ($N_{\text{MC}} = 128$ realizations for clarity), along with the theoretical mean energy $\langle E \rangle$ (yellow) and $\langle E \rangle \pm \Delta E$ (cyan), where ΔE^2 is the energy variance. Right: average occupation numbers n_k obtained for $N_{\text{MC}} = 128, 256$ realization, compared with the exact results (dashed lines).

is the number of bath degrees of freedom. Fig. S1 illustrates typical results of such sampling for the case considered in the main text, which used $F = 50$ harmonic oscillators with frequencies

$$\omega_k = -\omega_c \ln \left(\frac{k}{F+1} \right)$$

where ω_c is a cutoff frequency. This is a widely used discretization of the Ohmic bath with exponential cutoff, $J(\omega) = m\gamma\omega e^{-\omega/\omega_c}$, provided the couplings c_k with the system coordinate are set according to

$$c_k = \omega_k \sqrt{\frac{2}{\pi} \frac{m\gamma\omega_c}{F+1}} M$$

where m and M are, respectively, the system and the oscillators mass, and γ is the damping coefficient ($\gamma = \tilde{\eta}_0/m$, with $\tilde{\eta}_0$ being the static friction coefficient as defined in the main text.). Here, the cutoff frequency was set to $\omega_c = 500 \text{ cm}^{-1}$.

Importantly, we notice that the reagent partition function takes a form similar to the

total partition function

$$Z_A = Z_0 \sum_n \langle\langle W_{n,N}(\beta) \langle h_A \rangle_{n,N}^\beta \rangle\rangle \quad (8)$$

but now the system states are better chosen to closely resemble “the reagent states” since, in practice, a quickly convergent sum over n is highly desirable. In our implementation they are eigenstates of a fictitious Hamiltonian that describes reagents only, *i.e.* the states $|n\rangle$ are chosen to be eigenstates of $\tilde{H}_S = \frac{p^2}{2m} + \tilde{v}$ where \tilde{v} is a modified potential with the “reaction channel artificially closed”. This choice improves much the Monte Carlo convergence and, in practice, requires 1-2 system states (depending on the temperature) to obtain a numerically converged value of the reagent partition function. Notice further that the convergence depends also on other numerical parameters. For instance, a grid for the bath oscillations that is “centered” around the classical equilibrium position (the reagent minimum of the potential) is much more efficient than an “unbiased” grid (like the one appropriate for the flux evaluation). That is, for the typical Hamiltonian

$$H = H_S + \sum_k \left[\frac{p_k^2}{2M} + \frac{M\omega_k^2}{2} \left(x_k - \frac{c_k s}{M\omega_k^2} \right)^2 \right]$$

the center of the grid for the k^{th} harmonic oscillator is better placed at

$$x^\ominus = \frac{c_k}{M\omega_k^2} s_{\min}$$

where s_{\min} is the value of the system coordinate at the bottom of the reagent well.

2. Flux-side correlation

The standard flux-side correlation $C_{\text{fs}}^\beta \equiv \text{Tr}(e^{-\frac{\beta}{2}H} F e^{-\frac{\beta}{2}H} h(t))$ can be evaluated similarly to the expectation values considered above by introducing the spectral representation of $F = \sum_u u |u\rangle \langle u|$ and re-writing the trace as a sum over states

$$C_{\text{fs}}^\beta(t) = \sum_u \sum_N u \langle uN | h(\tau) | uN \rangle$$

where the expectation of the operator $h(\tau) = e^{\frac{i}{\hbar}H\tau^*} h e^{-\frac{i}{\hbar}H\tau}$ (with $\tau = t - i\frac{\hbar\beta}{2}$) requires both the imaginary and the real time evolution. This general procedure is, however, numerically inconvenient since F (albeit *system-only*) has many contributing eigenstates, thereby making the sum over u rather long⁹. Fortunately, at least for the case we are interested in, there is

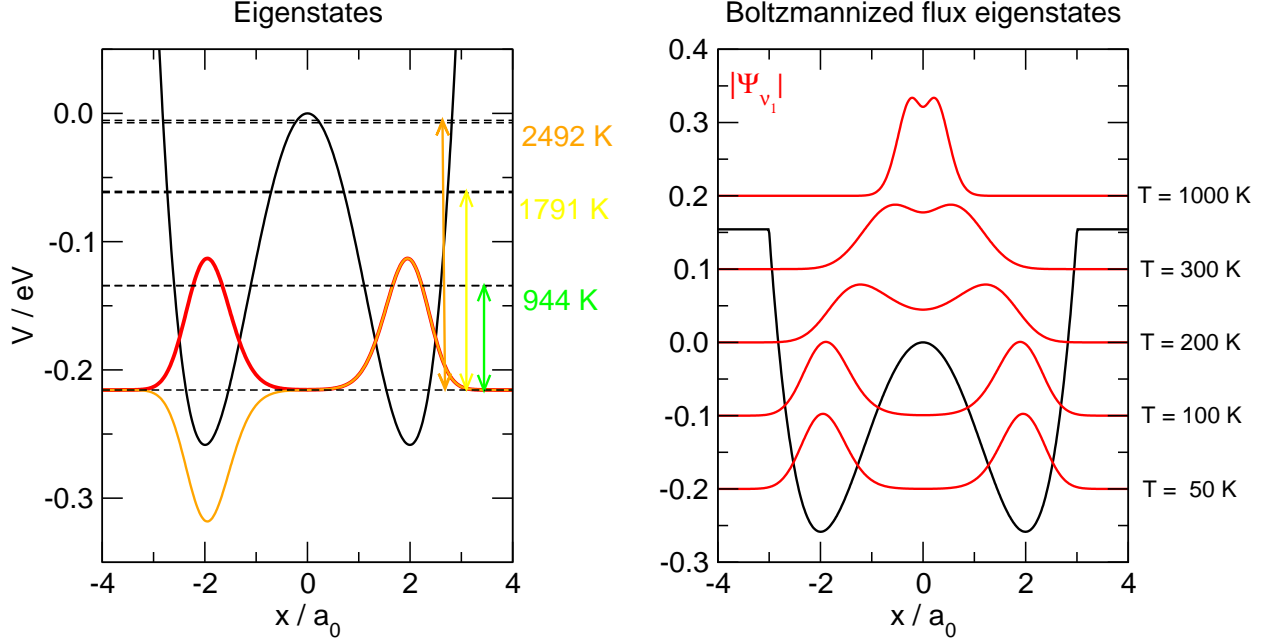


FIG. S2: Boltzmannized flux eigenstates $|\nu_\beta\rangle$ for a symmetric double well potential (black curves). Left: the two lowest-lying energy eigenstates forming the ground-state tunneling-split doublet. Right: the absolute value of the Boltzmannized-flux eigenfunction with the largest positive eigenvalue, as obtained at the indicated temperatures (vertically shifted for clarity). a_0 refers to the Bohr radius.

a way out of this “dimensionality” problem: the *Boltzmannized* flux operator is intrinsically of low-rank, that is it reads as

$$F_\beta^S = e^{-\frac{\beta}{2}H_S} F e^{-\frac{\beta}{2}H_S} = \sum_\nu \nu(\beta) |\nu_\beta\rangle \langle \nu_\beta|$$

where only few values of $\nu(\beta)$ ’s are significant (in fact just two, related to each other by time inversion, if the temperature is low enough, as it easily follows by the two-state approximation of the dynamics)¹⁰. Fig. S2 illustrates the typical behavior of the most important flux eigenstates at varying temperatures, and their relation to the energy eigenstates. To exploit the above property, following Craig *et al.*⁶, we write

$$\begin{aligned} F &= e^{+\frac{\beta}{2}H_S} F_\beta^S e^{+\frac{\beta}{2}H_S} = \sum_\nu \nu(\beta) e^{+\frac{\beta}{2}H_S} |\nu_\beta\rangle \langle \nu_\beta| e^{+\frac{\beta}{2}H_S} \\ &\equiv \sum_\nu w_\nu(\beta) |\bar{\nu}_\beta\rangle \langle \bar{\nu}_\beta| \end{aligned}$$

where $|\bar{\nu}_\beta\rangle$ are normalized, imaginary-time backward-propagated flux eigenvectors,

$$|\bar{\nu}_\beta\rangle = \frac{1}{\sqrt{\langle \nu_\beta | e^{\beta H_S} | \nu_\beta \rangle}} e^{\beta H_S/2} |\nu\rangle$$

and $w_\nu(\beta) = \nu(\beta) \langle \nu_\beta | e^{\beta H_S} | \nu_\beta \rangle$ are flux-weights. The $|\bar{\nu}_\beta\rangle$'s are non-orthogonal, yet rather useful since they provide a compact representation of the flux operator. With these definitions, we have

$$\begin{aligned} C_{\text{fs}}^\beta &= \sum_\nu \text{Tr} \left(e^{-\beta H/2} |\bar{\nu}_\beta\rangle \langle \bar{\nu}_\beta| e^{-\beta H/2} h(t) \right) w_\nu(\beta) \\ &\equiv \sum_\nu \sum_N w_\nu(\beta) \langle \bar{\nu}_\beta N | e^{-\beta H/2} h(t) e^{-\beta H/2} | \bar{\nu}_\beta N \rangle \end{aligned}$$

and everything proceeds as above. Specifically, introducing the normalized vectors

$$|\Phi_{\nu,N}^\beta\rangle = \frac{1}{\sqrt{p_{\nu N}(\beta)}} e^{-\beta H/2} |\bar{\nu}_\beta N\rangle, \quad p_{\nu N}(\beta) = e^{-2 \int_0^{\beta/2} \epsilon_{\nu N}(\tau) d\tau},$$

their real-time evolutions

$$|\Phi_{\nu,N}^\beta(t)\rangle = e^{-\frac{i}{\hbar} H t} |\Phi_{\nu,N}^\beta\rangle$$

and the expectation $\langle h(t) \rangle_{\nu N}^\beta = \langle \Phi_{\nu,N}^\beta(t) | h | \Phi_{\nu,N}^\beta(t) \rangle$ we write

$$C_{\text{fs}}^\beta = Z_0 \sum_N \frac{e^{-\beta E_N}}{Z_0} \sum_\nu w_\nu(\beta) W_{\nu N}(\beta) \langle h(t) \rangle_{\nu N}^\beta,$$

where $W_{\nu N}(\beta) = p_{\nu N}(\beta) e^{\beta E_N}$ are thermal factors (Eq. 5) and $w_\nu(\beta)$ are (thermal) flux weights. Equivalently,

$$C_{\text{fs}}(t) = Z_0 \sum_\nu \langle\langle w_\nu(\beta) W_{\nu N}(\beta) \langle h(t) \rangle_{\nu N}^\beta \rangle\rangle \quad (9)$$

is the working expression involving

- (i-a) a “system” preparation to define the appropriate system states $|\bar{\nu}_\beta\rangle$,
- (i-b) a Monte Carlo sampling of the (uncoupled) bath state, which delivers bath states $|N\rangle$,
- (ii) a relaxation dynamics with the full Hamiltonian H for each state $|\bar{\nu}_\beta N\rangle$
- (iii) a real time dynamics with the same Hamiltonian on the relaxed states obtained in (ii).

When combined with the calculation of the reagent partition function, Eq. 8, this recipe gives the thermal rate constant of Eq. 4 or, with minor additional effort, the one defined by Eq. 1.

In closing this section it is worth noticing that the manipulations above with the Boltzmann operator are well defined when the Hamiltonian operator H_S is bound¹¹ but some regularization is needed when — as it is often the case in realistic problems — the spectrum of H_S is unbound. This is particularly important for numerical applications because the presence of high-lying energy eigenstates makes $\exp(-\beta H_S)$ nearly singular and $\exp(+\beta H_S)$ numerically unstable, increasingly so when reducing the temperature ($\beta \rightarrow \infty$). Fortunately, such high-lying energy eigenstates should not play any role in the dynamics (particularly at the low temperatures where a quantum description is required) and the simple regularization of replacing H_S with its projection \bar{H}_S on a low-lying energy eigenspace suffices. Specifically, defining P_n the projection onto the first (lowest lying) n eigenstates of H_S one defines $\bar{H}_S = P_n H_S P_n$ and uses it in place of H_S in some of the expressions above. This is entirely legitimate since the aim is just to re-write F in a suitable way, but of course one must ensure that \bar{H}_S closely resembles H_S for the expansion to be compact. In practice, then, one uses H_S to define the Boltzmannized flux and diagonalize it, and then switches to \bar{H}_S when propagating backward in imaginary time, making sure that the “error” is kept below a desired threshold^{12,13}.

C. ML-MCTDH wavefunction and calculation setup

Fig. S3 shows the tree structure defining the ML-MCTDH wavefunction. It was obtained after extensive testing, and found to accurately reproduce previous ML-MCTDH and PI results, at both high and low temperatures at varying coupling strengths, ranging from the weak to the strong coupling limits. The number of logical modes used in each layer was kept small (2 – 3) and each of them was described with several single-particle functions (12 – 6). Only in the bottom layer, depending on the size of the primitive grids, the bath degrees of freedom (the “ q_k ”s in Fig. S3, sorted in order of increasing frequency) were grouped in 3 – 4 dimensional single-particles. The system mode (the “ x ” in Fig. S3) is located in the group of bath modes with comparable frequency, although described separately from the bath modes and with the help of a large number of SPFs. As for the primitive grids we

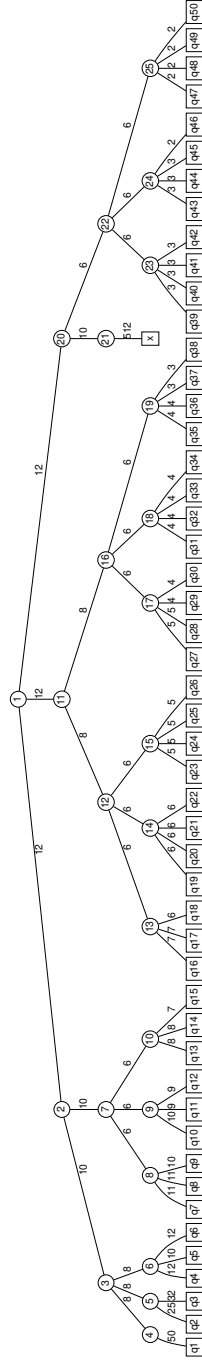


FIG. S3: Adopted tree structure for the ML-MCTDH wavefunction. Each circle denotes a MCTDH-like expansion in the tree, along with its modes (the arms) and the number of the single particle functions used in the expansion (the numbers on the arms). Squares denote the bottom layers where modes reduce to physical degrees of freedom and the numbers represent the size of the primitive grids. Here x is the system coordinate and the q_k 's are bath coordinates.

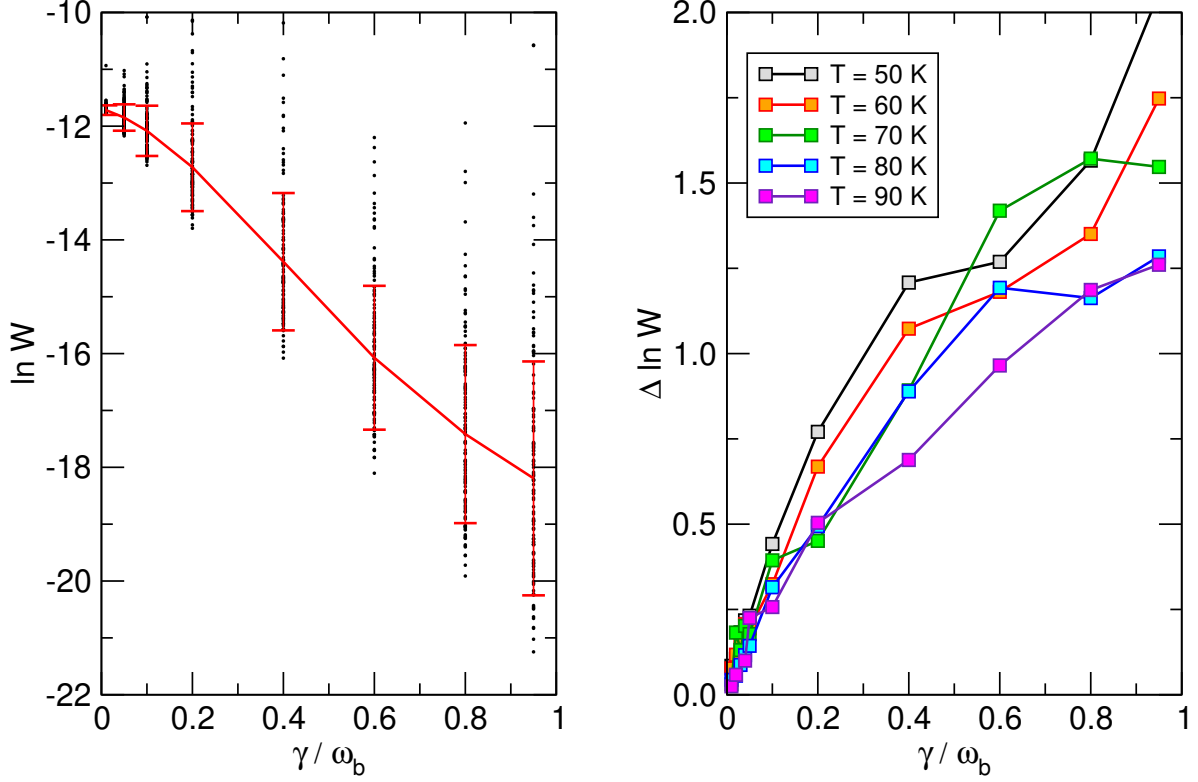


FIG. S4: Behavior of the thermal factors obtained in thermalization step. Left: individual realizations, with their average and root mean square given as red curve with error bars. Right: root mean square for different temperatures, as a function of the coupling strength.

used Harmonic Oscillator - Discrete Value Representation (HO-DVR) grids for each bath degrees of freedom, which amounts to introduce a phonon basis of the same size for the corresponding mode. The grids for the low frequency modes used several tens of points (as indicated in Fig. S3), and were extended if necessary to accommodate each realization sampled from the canonical ensemble of the bath. The grids for the high-frequency modes, on the other hand, used much fewer grid points since they were barely excited during the dynamics. The system degree of freedom was described with a uniformly spaced grid, a Fast Fourier Transform - Discrete Value Representation (FFT-DVR), using 512 grid points in the range $x \in [-4, 4] a_0$ (with a_0 referring to the Bohr radius).

The MCTDH equations of motion were integrated with the Variable Mean Field scheme, using a variable step-size 8th-order Runge-Kutta integrator for both the amplitude coefficients and the single-particle wavefunctions, and a small accuracy parameter (10^{-8}). The propagation time was set differently according to the coupling strength, in order to guar-

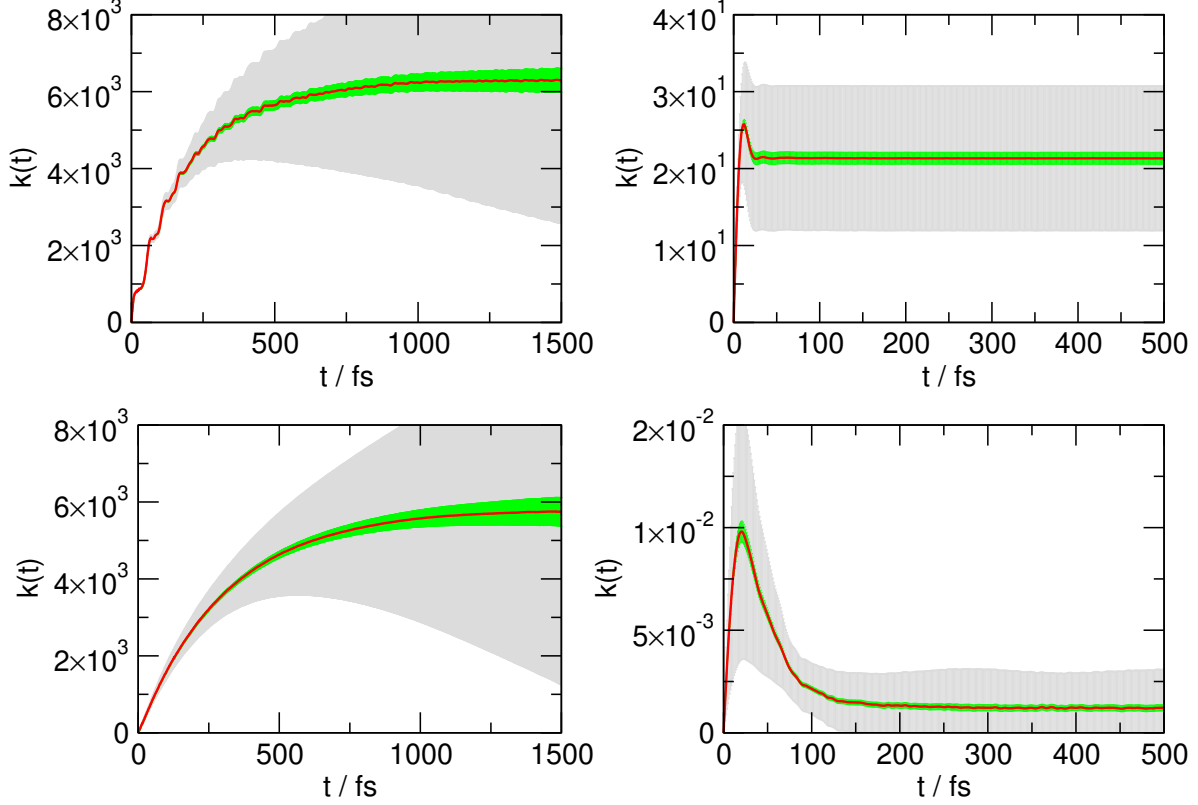


FIG. S5: Illustrative examples showing the behavior of the flux-side correlation function at $T = 90$ K (top row) and $T = 50$ K (bottom row), for very small and large coupling strength, $\gamma/\omega_b = 0.01$ and 0.95 , respectively for the left and right panels. Gray (green) area shows the spread (statistical error) calculated as the root-mean-square deviation of x_N (root-mean-square deviation of x_N over square-root of number of realizations).

ante that the computed flux-side correlation functions attained a constant limiting value (which occurs at increasingly longer times when decreasing friction). Similarly, the number of realization was chosen differently depending on the considered temperature and coupling strength, the higher T and/or γ the larger the number of realizations used. Fig. S4 shows the behavior of the thermal factors of Eq. 5 as computed in the “equilibration step” (step ii above), which are the weights with which the individual realizations of the bath enter into the flux-side correlation function expression of Eq. 9 (for a given flux state). Their logarithms are within $0 - 2$ over a wide range of coupling strengths, meaning roughly that each realization has a weight in a two-order-of-magnitude wide interval at most. Fig. S5, on the other hand, displays some illustrative examples of the evolution of the correlation functions, along with the spread of the contributing terms in the sum of Eq. 9. More specifically, the

latter was obtained by grouping results from opposite flux eigenvalues, and rewriting Eq. 9 as an average of individual contributions $x_N = \sum_{\nu} W_{\nu N} |w_{\nu}(\beta)| \left[\langle h \rangle_{+|\nu|,N} - \langle h \rangle_{-|\nu|,N} \right]$ with a spread given by the root-mean-square deviation of the x_N 's. Hence, provided bath sampling is sufficiently extended, it measures the intrinsic variability of the reaction probability across the thermal equilibrium state.

III. CONVERGENCE TESTS OF DFT CALCULATIONS

A. Energy Barriers

In Fig. S6 the convergence of the energy with respect to k-grid sampling for the hydrogen hopping reaction in Pd is shown. It can be observed that a 6x6x6 k-grid with *light* settings delivers converged results for the reaction energy and energy barrier for the 2x2x2 supercell. The corresponding values obtained for the 1x1x1 supercell show a considerably larger reaction energy and barrier height.

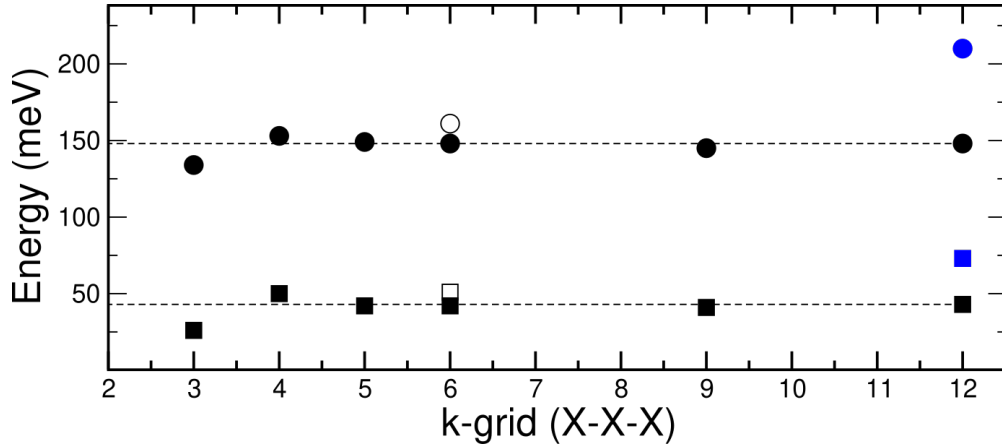


FIG. S6: Reaction energy, $E_T - E_O$, and energy barrier heights, $E_{SP} - E_O$, for Pd are represented by squares and circles, respectively. E_T , E_O , and E_{SP} refer to the potential energy corresponding to structures where the H atom is located at the tetrahedral (T), octahedral (O) and saddle-point (SP) sites, respectively. Values reported without ZPE correction. Calculations were performed using supercells constructed from 2x2x2 (black) and 1x1x1 (blue) copies of the cubic unit cell. Dashed lines are shown as a guide to the eye. Standard *light* with a modified radial multiplier=2 (filled symbols) and *tight* (empty symbols) settings from FHI-aims were used.

B. Friction Calculations

1. *k*-grid Convergence

Fig. S7 shows the convergence of the friction tensor on the hydrogen on different positions with respect to *k*-grid sampling. The friction eigenvalues converged within 20 % and 3 % with *k*-grid of 6x6x6 and 15x15x15, respectively.

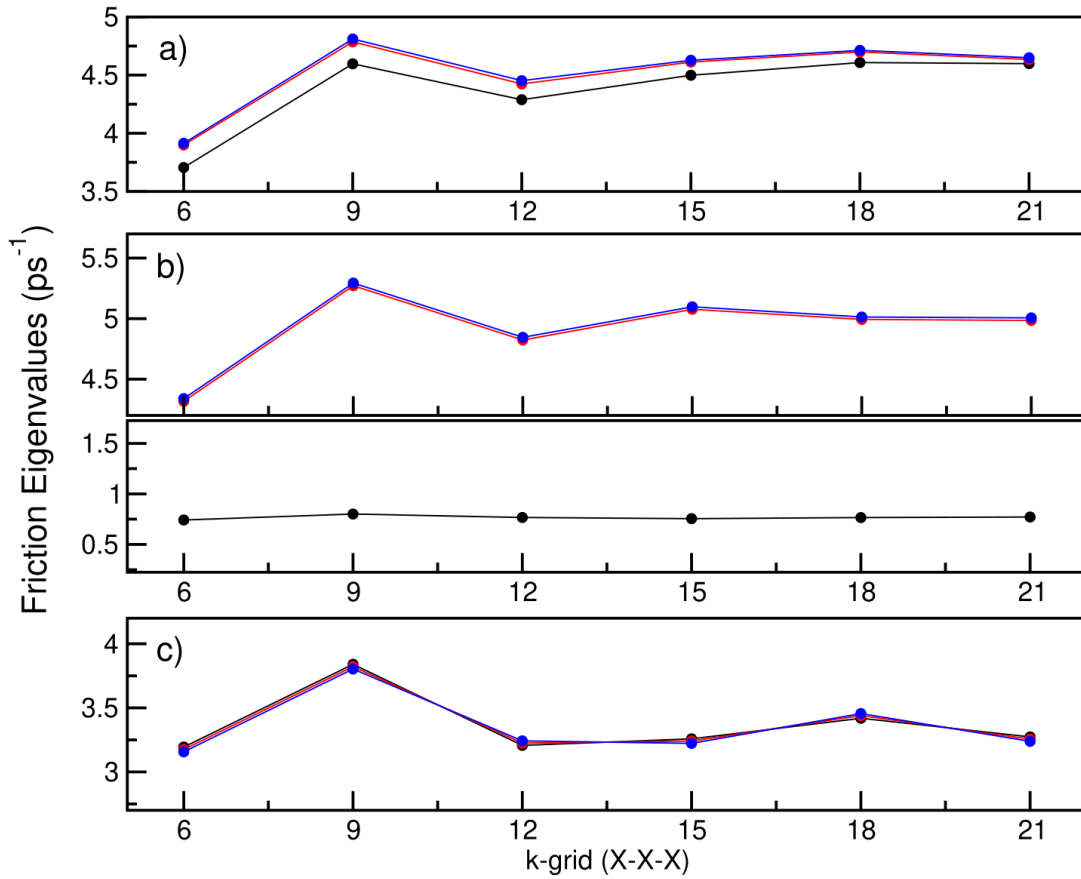


FIG. S7: Convergence of eigenvalues of the friction tensor on the hydrogen atom for Pd_{32}H for a) tetrahedral site, b) transition state between tetrahedral and octahedral sites, and c) octahedral site. Standard *light* from FHI-aims were used with a modified radial multiplier=2 (filled symbols) were used. A broadening of 0.05 eV was used and the reported values are evaluated in the static limit. The different colours represent the three eigenvalues (one unique and two degenerate).

2. Displacement Convergence

Fig. S8 shows the convergence of the friction tensor with respect to the displacement length used in the finite difference calculation. The friction eigenvalues vary by less than 5% in the 0.5×10^{-3} to 4×10^{-3} Å range.

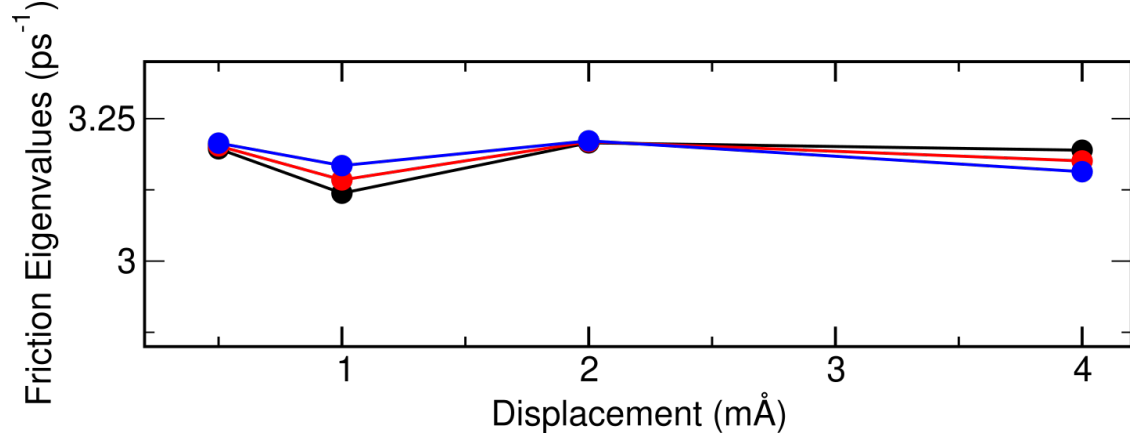


FIG. S8: Convergence of eigenvalues of the friction tensor on the hydrogen atom with respect to displacement length for the hydrogen atom on the octahedral site (Pd_{32}H). A k-grid of 6x6x6 has been used and other settings were set equal to the k-grid convergence test.

3. Friction along the Minimum Energy Pathways

In Fig. S9-S12, the friction value projected along the minimum energy path together with the minimum energy pathway (MEP) are presented.

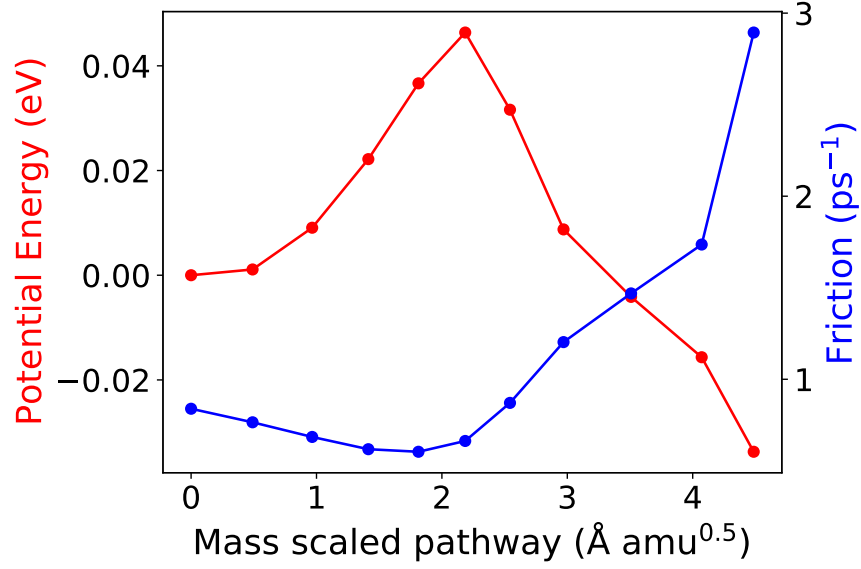


FIG. S9: Electronic friction (Eq. 9 in the main text) and potential energy along the minimum energy pathway for Pt. The former computed only for the hydrogen atom and it is projected along the reaction coordinate. Octahedral \rightarrow tetrahedral transition is considered.

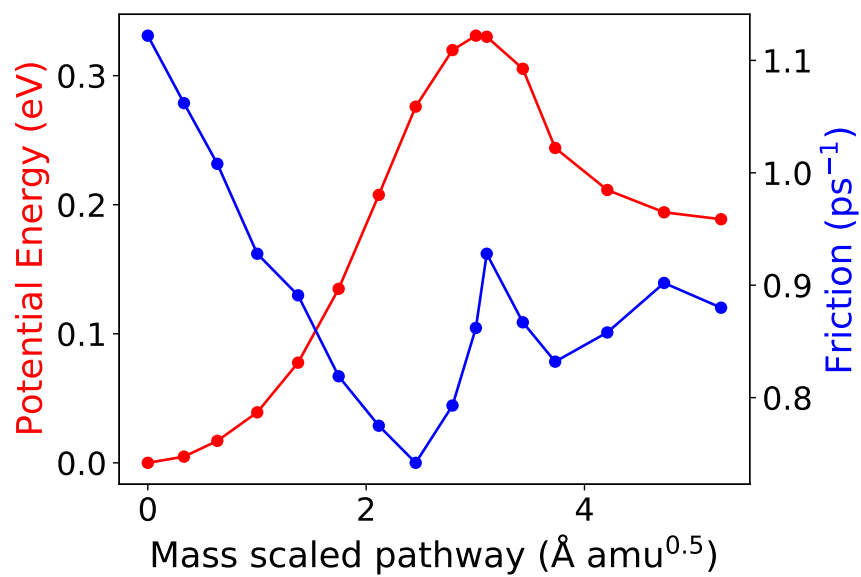


FIG. S10: Same as S9 for Cu.

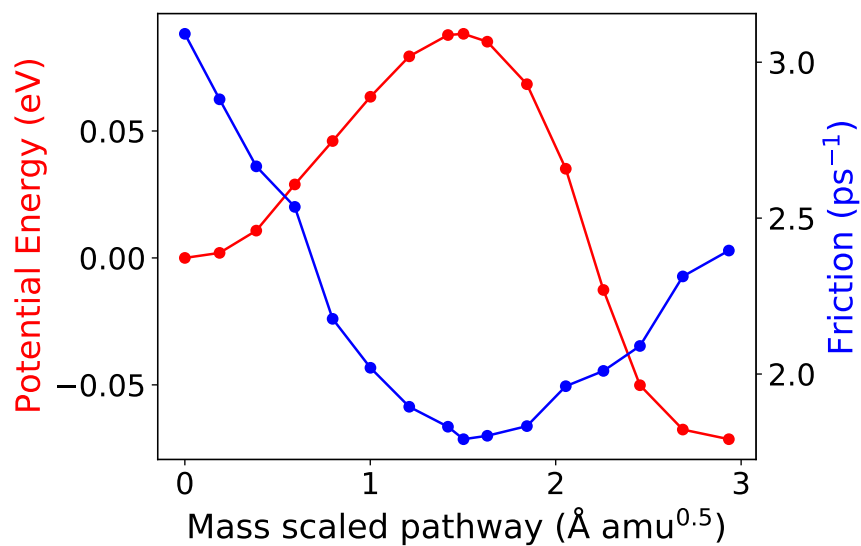


FIG. S11: Same as S9 for Al.

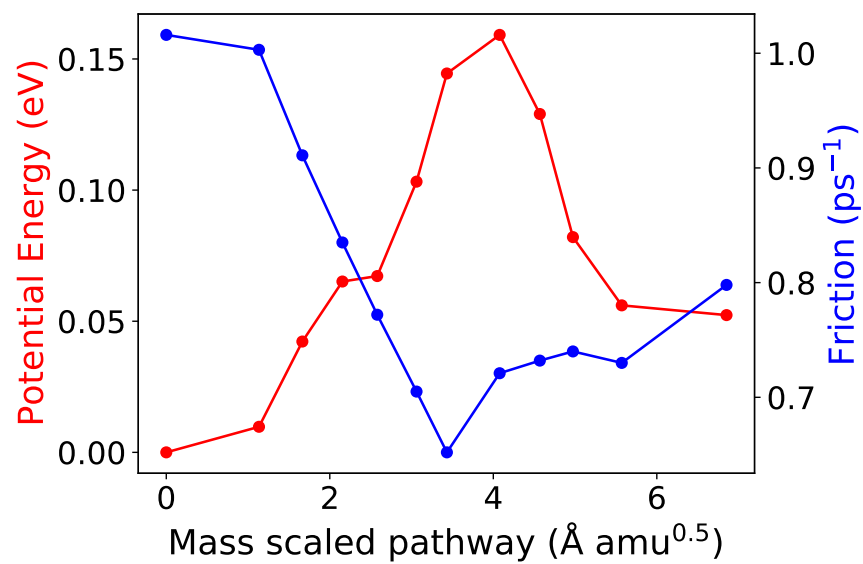


FIG. S12: Same as S9 for Ag.

4. Frequency dependence of Electronic Friction

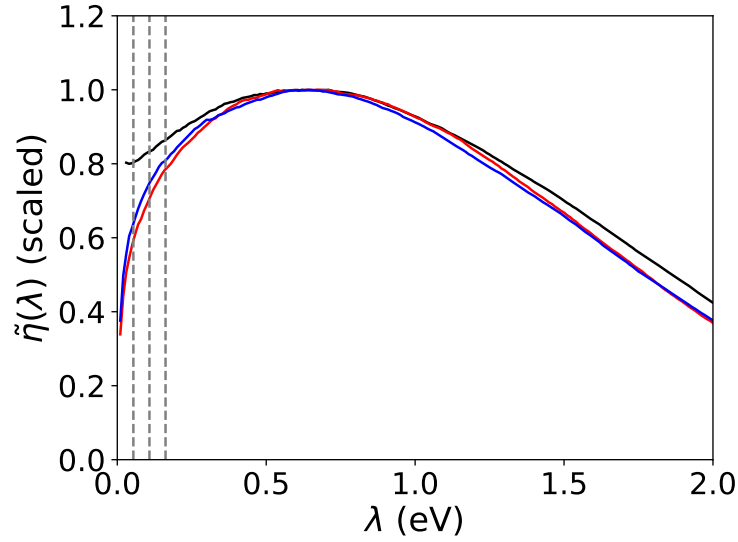


FIG. S13: Frequency dependence of the friction tensor (Eq. 11 in the main text) projected on the reaction coordinate at the reactant (black), transition state (red), and product (blue) states for Pt. The first three non-zero ring-polymer normal modes frequencies at 100K are depicted as vertical dashed gray lines. To ease visual comparison, all curves in panel have been scaled to adopt the value of 1 at the frequency of the first local maximum.

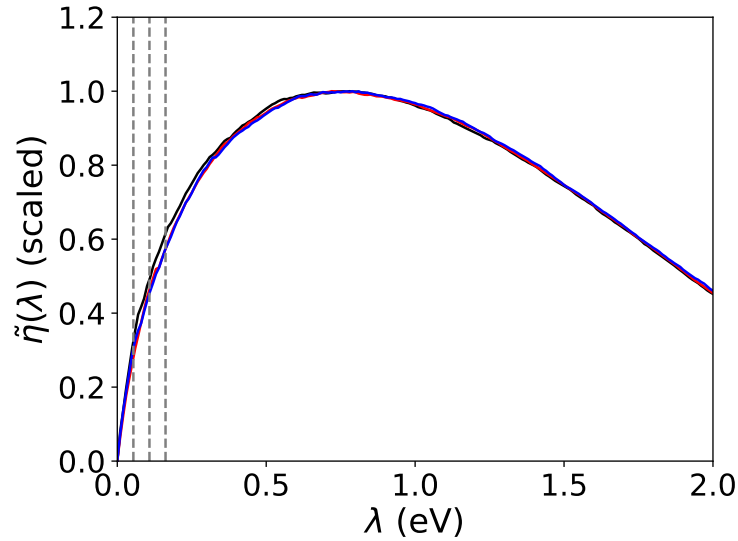


FIG. S14: Same as S13 for Al

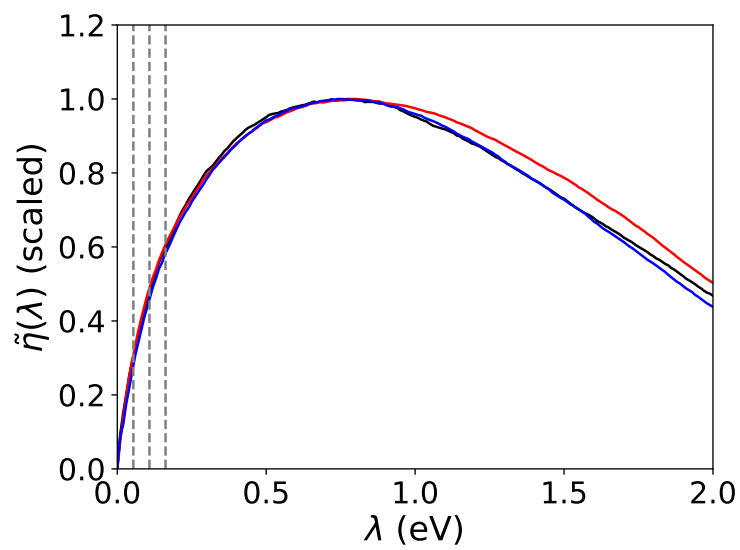


FIG. S15: Same as S13 for Cu

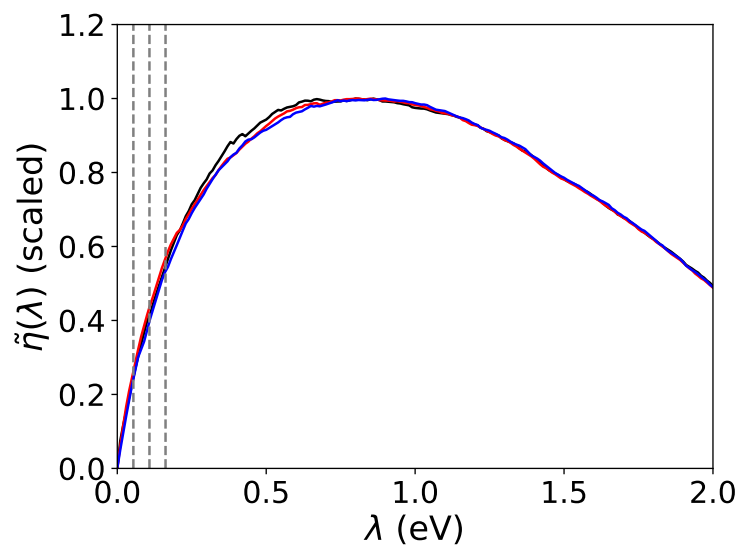
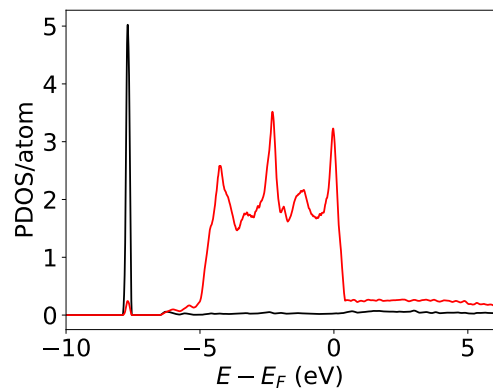


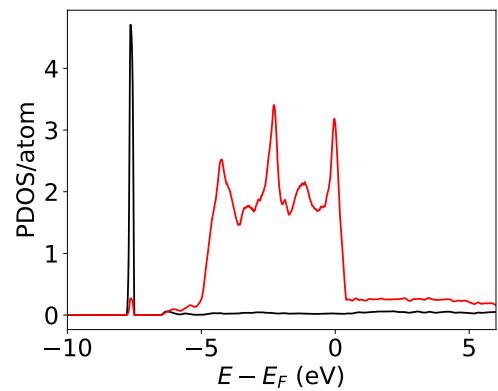
FIG. S16: Same as S13 for Ag

C. Analysis of Projected Density of States

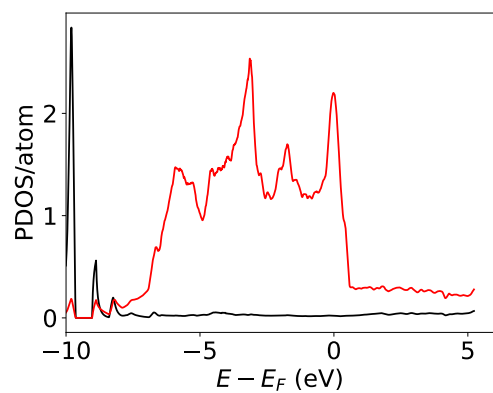
In Fig. S17 and S18 we show the projected density of states (PDOS) for all the systems considered in this work. These calculations were performed with a $16 \times 16 \times 16$ k-point sampling as used for the friction tensor calculations.



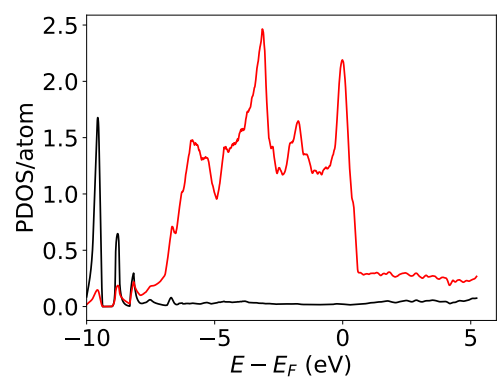
(a) H@Pd reactant geometry



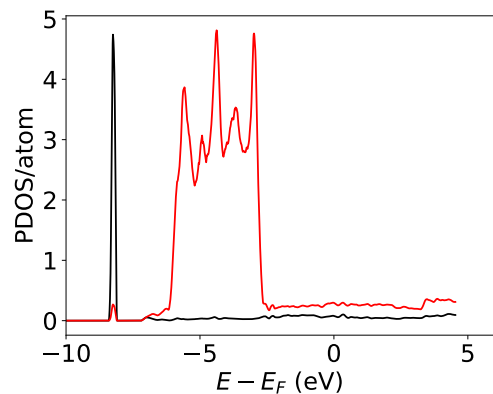
(b) H@Pd transition state geometry



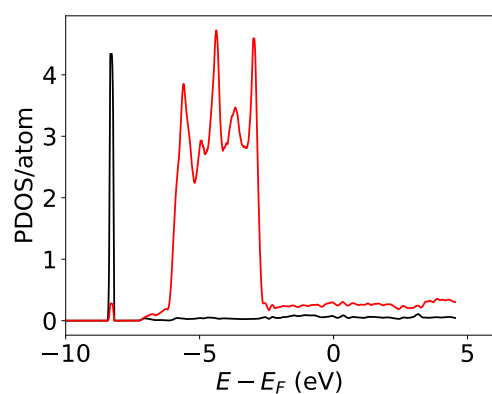
(c) H@Pt reactant geometry



(d) H@Pt transition state geometry

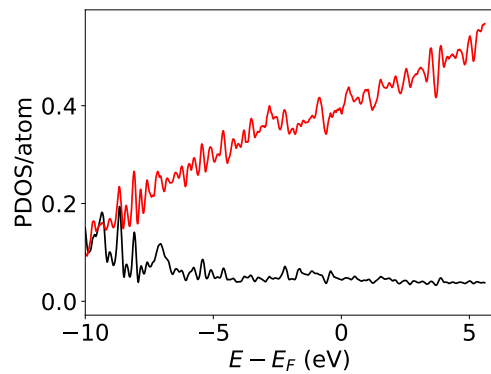


(e) H@Ag reactant geometry

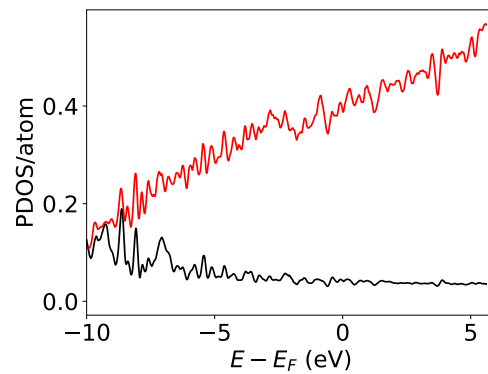


(f) H@Ag transition state geometry

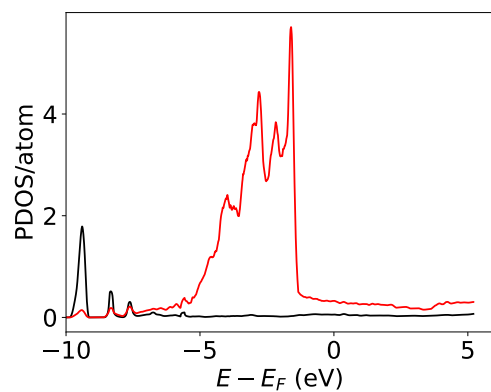
FIG. S17: Projected density of states (PDOS) on H (black) and X (red) atoms for X=Pt, Ag.



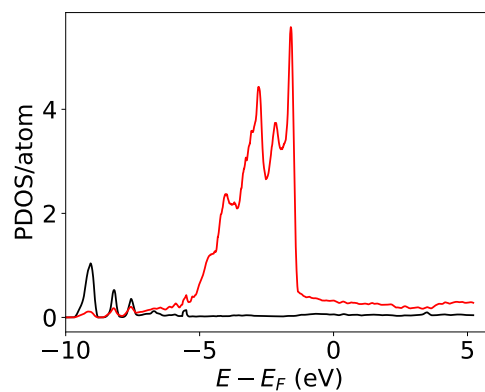
(a) H@Al reactant geometry



(b) H@Al transition state geometry



(c) H@Cu reactant geometry



(d) H@Cu transition state geometry

FIG. S18: Projected density of states (PDOS) on H (black) and X (red) atoms for X=Cu,
Al

IV. ACCURACY OF RATE ESTIMATION FOR ASYMMETRIC DOUBLE WELL POTENTIAL

Fig. S19 shows the error incurred by the application of the extension of the Grote-Hynes type approximation into the deep tunneling regime an asymmetric double well potential. Similarly to what is observed for a symmetric double well potential in the main text, the error increases with the increase of the friction, the increase of the barrier height, and/or the decrease of the temperature. Except for the highest barrier and friction value at the lowest temperature considered, all the estimated rates are within 1 order of magnitude of the reference values.

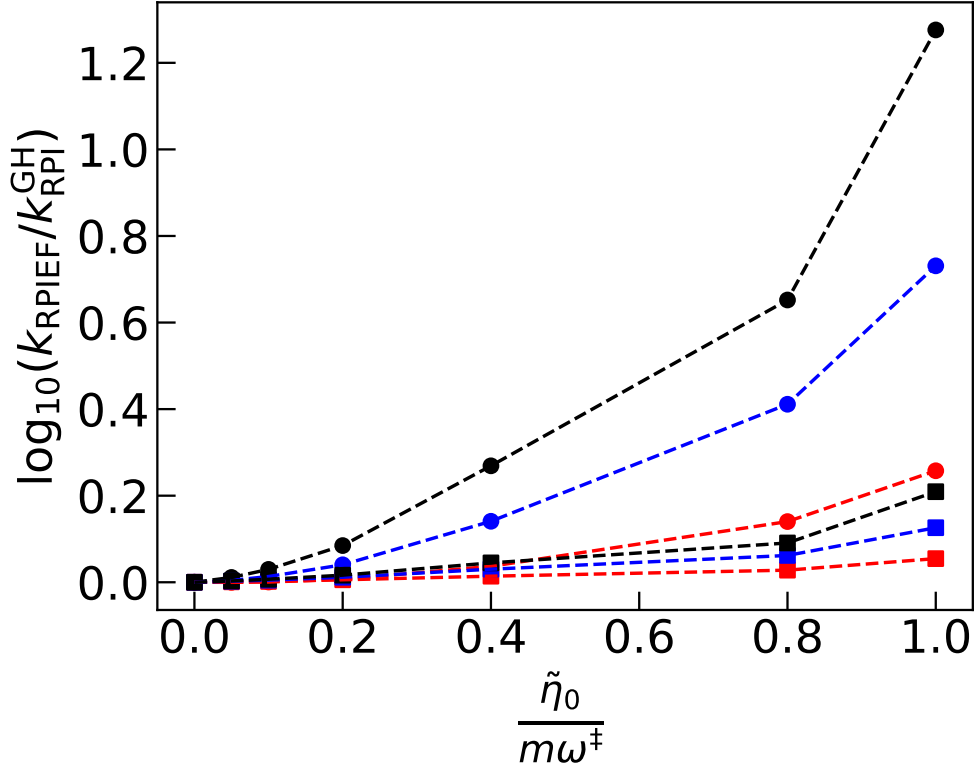


FIG. S19: Error of the RPI rate values obtained by the scaling relation shown in Eq. 13 of the main text ($k_{\text{RPI}}^{\text{GH}}$), compared to the RPI-EF rates ($k_{\text{RPI-EF}}$) for an asymmetric double well model ($q_0=0.08 \text{ \AA}$) at $0.70T_c^\circ$ (squares) and $0.55T_c^\circ$ (circles) for reaction barriers of 258 meV (red), 500 meV (blue), and 1000 meV (black). The error is reported as the ratio of these rates. Analogous plot is presented in main text for a symmetric barrier model.

REFERENCES

- ¹Y. Litman, *Tunneling and Zero-Point Energy Effects in Multidimensional Hydrogen Transfer Reactions: From Gas Phase to Adsorption on Metal Surfaces*, Ph.D. thesis, Freie Universität Berlin (2020).
- ²T. Yamamoto, The Journal of Chemical Physics **33**, 281 (1960).
- ³W. H. Miller, S. D. Schwartz, and J. W. Tromp, The Journal of Chemical Physics **79**, 4889 (1983).
- ⁴W. H. Miller, Journal of Physical Chemistry A **102**, 793 (1998).
- ⁵A. N. Drozdov and S. C. Tucker, The Journal of Chemical Physics **115**, 9675 (2001).
- ⁶I. R. Craig, M. Thoss, and H. Wang, J. Chem. Phys. **127**, 144503 (2007).
- ⁷H. Wang, D. E. Skinner, and M. Thoss, The Journal of Chemical Physics **125**, 174502 (2006).
- ⁸I. R. Craig, M. Thoss, and H. Wang, Journal of Chemical Physics **127** (2007), 10.1063/1.2772265.
- ⁹Notice that the total number of wavepackets is given by $M \times N_{\text{MC}}$, where M is number of contributing system states and N_{MC} the size of the Monte Carlo ensemble for the bath, typically $N_{\text{MC}} = 128 - 256$.
- ¹⁰Notice that F here is a *system-only* operator and that the above expression is of low rank only in the space of system states \mathcal{H}_S : when the same operator is considered in the whole space \mathcal{H} each eigenflux space becomes highly degenerate.
- ¹¹When a maximum eigenvalue exists the Boltzmann operator is non-singular.
- ¹²The reliability of such regularization can be measured by the difference in the (differently) Boltzmannized flux eigenvalues and by two kinds of errors in the flux eigenstates: there exists a *truncation* error (the distance between the eigenvectors of the differently Boltzmannized operators) and a *propagation* error (defined by back-propagating with the “projected version” of the Boltzmann operator followed by propagation with the true Boltzmann operator). The latter two behave oppositely when varying n since the truncation error determines the quality of the projected Hamiltonian and the propagation error reflects the above mentioned numerical instability.
- ¹³There is no need for H_S to be the same “system” Hamiltonian appearing in the total Hamiltonian, and one can set it at his own convenience. After all the flux operator F does

not depend on the potential.